

A Progress Report for NAGW-9

A Study of Physical Mechanisms for Filament Eruption  
and Coronal Mass Ejection Via Numerical Simulation

January 1, 1991 - June 1991

Prepared by

S. T. Wu

Department of Mechanical Engineering  
and Center for Space Plasma and Aeronomic Research  
The University of Alabama in Huntsville  
Huntsville, AL 35899

(NASA-CR-192118) A STUDY OF  
PHYSICAL MECHANISMS FOR FILAMENT  
ERUPTION AND CORONAL MASS EJECTION  
VIA NUMERICAL SIMULATION Progress  
Report, 1 Jan. - Jun. 1991  
(Alabama Univ.) 50 p

N93-18577

Unclass

G3/92 0143808

14507

P.50

1N-92-CN  
143808

P- 47

## Table of Contents

|   |    |
|---|----|
| I. Work completed (published and accepted for publication) .....                                    | 1  |
| II. Work In Progress .....  | 1  |
| II.1. Critical shear study .....  | 1  |
| II.2. Improved PEM for the extrapolation of the nonlinear force-free field .....                    | 2  |
| II.3. Study of emerging flux from sub-photospheric layer .....                                      | 5  |
| III. Tasks for the Third Year Grant (January 1, 1992 - December 31, 1992) .....                     | 15 |
| III.1. Radiation and thermal conduction effects on nonlinear evolution of critical equilibria ..... | 15 |
| III.2. Quantitative analysis of the 1989 March flares .....   | 15 |
| III.3. Study the energy and momentum transport from the sub- photospheric layer                     | 15 |
| III.4. Assessment of the study .....  | 15 |
| References .....  | 15 |
| Appendix .....  | 19 |
| Attachments .....   | 22 |

Since the renewal of this grant (NAGW-9) in January 1991, the research has progressed smoothly according to the plan in the original proposal with some modifications (see Appendix A). The significant achievements during this period are described in the following:

## **I. Work completed (published and accepted for publication)**

1. S. T. Wu and Ai-Hwa Wang, "Numerical Simulation of Extended Corona", 1991, Adv. Space Res., Vol. 11, No. 1, 187.
2. Tyan Teh and S. T. Wu, "Model Calculations of the Rising Motion of a Prominence Loop", 1991, Solar Physics, 132, 335.
3. S. T. Wu, M. T. Song, P. C. H. Marten, and M. Dryer, "Shear Induced Instability and Arch Filament Eruption: A Magnetohydrodynamic (MHD) Numerical Simulation", 1991, Solar Physics, (in press).
4. S. T. Wu, M. T. Song and E. Tandberg-Hanssen, "A Numerical Simulation of Atmospheric Responses Due to Emerging Flux From Sub-Photospheric Layers", Bull. American Astronomical Society, (Abstract) Solar Physics Division Meeting, Huntsville, AL, April 1991.
5. M. T. Sun, S. T. Wu, F. S. Weng, and M. T. Song, "Further Numerical Tests for the Progressive Extension Method (PEM) for Extrapolation of Solar Force- Free Magnetic Field", Bull. American Astronomical Society, (Abstract) Solar Physics Division Meeting, Huntsville, AL, April 1991.

A copy of these reprints and abstracts are attached.

## **II. Work In Progress**

The work currently in progress is summarized in the following:

### **II.1. Critical shear study**

It is well-known from both observation and theory that photospheric shear motion has played a key role in physical processes of the energy build-up and release for the solar flare. In order to further our understanding of the occurrence of solar flares it is necessary to investigate the triggering mechanism. One popular scenario for the onset of eruptive solar flares is that in response to photospheric shear motions the magnetic field evolves slowly through a series of magnetohydrodynamic-equilibria until a threshold is reached where magnetohydrodynamic (MHD) non-equilibrium sets in. Thus, a magnetic eruption occurs, causing the solar flare.

To substantiate this claim we have employed our newly developed three- dimensional, time-dependent MHD code with gravity to simulate the evolution of the coronal field.

We use plasma  $\beta = 0.1$  to closely approximate the condition in the actual corona. Some preliminary results are shown in Figures 1 and 2. Figure 1 shows the time sequence of the evolving magnetic field configuration in three-dimensions due to the photospheric motion. Figure 2 shows the density enhancement and magnetic field line projected on the  $x - z$  plane. In this presentation (Figure 2), we observe the following interesting features:

- (i) MHD waves (fast and slow modes) were generated due to the photospheric shear motions. Fast-mode waves propagate upward and slow mode waves propagate along the field lines.
- (ii) A current was also generated and moves upward slowly.

Presently, we have begun to analyze these results in detail to reveal the physical processes in these data.

## II.2. Improved PEM for the extrapolation of the nonlinear force-free field

Since the publication of the first version of our extrapolation scheme (Wu et al. 1990), called "Progressive Extension Method (PEM)", further improvement was made on the regularization techniques. This new regularization technique can be summarized as follows: the expression for averaging given by Eqs. (3.5) and (3.6) of the paper by Wu et al. (see Appendix) is modified as follows:

The regularized solution  $\bar{B}'_{i,j}$  becomes

$$\bar{B}'_{i,j} = (1 - \gamma)B_{i,j} + \gamma\bar{B}_{i,j} \quad (1)$$

where  $\bar{B}_{i,j}$  is the same as Eq. (3.5) and

$$\gamma(z) = \gamma_0 \exp[a(z/z_{max})] \quad (2)$$

with  $\gamma_0$  being arbitrary and which will be determined by trial and error method until the solution converges and

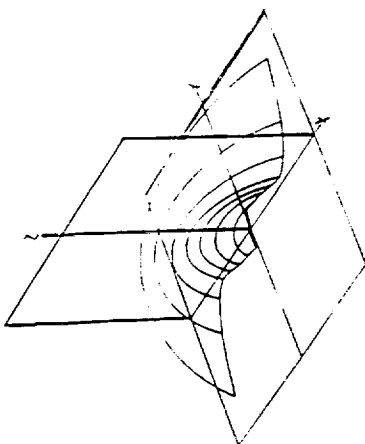
$$a = \ln(\gamma(z_{max})/\gamma_0) \quad (3)$$

By setting our goals on  $\gamma(z_{max})$  and  $\gamma_0$ ,  $a$  is determined.

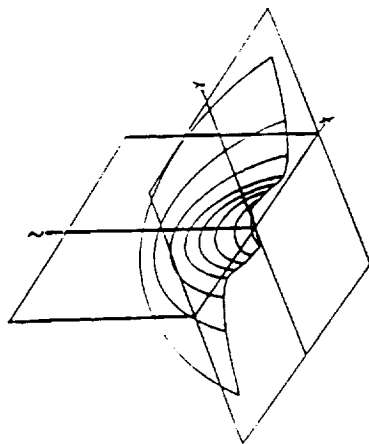
Using this modified technique, we perform a number of tests by using a rather complicated analytical nonlinear force-free solution (Low and Lou, 1990) as the input to the

# The Evolution of Magnetic Arcades (Numerical, $C=0.40$ , $\text{Beta}=0.10$ )

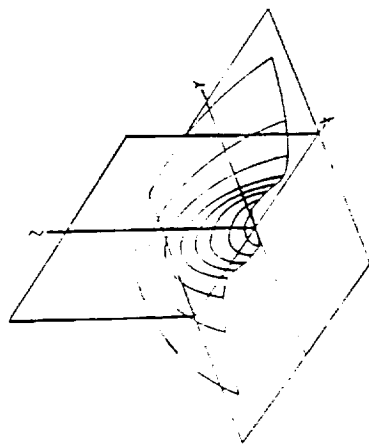
Time= 1.00% of Max Time



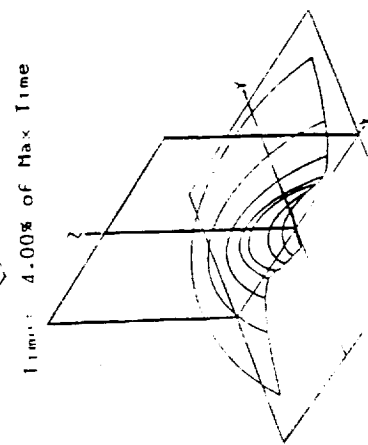
Time= 2.00% of Max Time



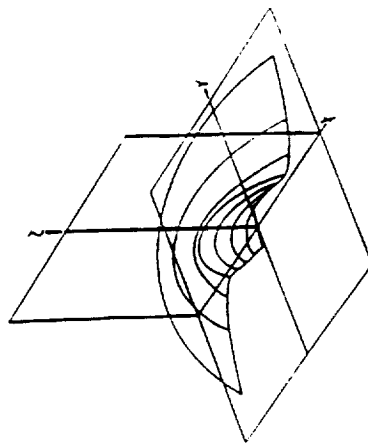
Time= 3.00% of Max Time



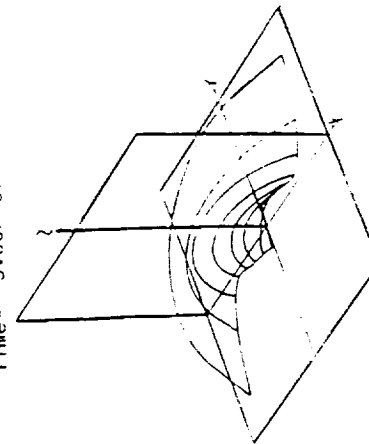
Time= 4.00% of Max Time



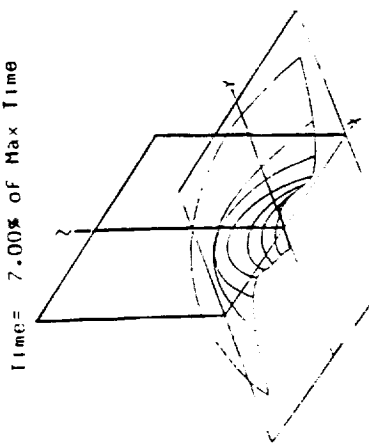
Time= 5.00% of Max Time



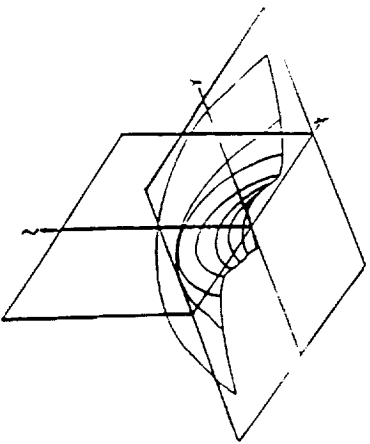
Time= 6.00% of Max Time



Time= 7.00% of Max Time



Time= 8.00% of Max Time



Time= 9.00% of Max Time

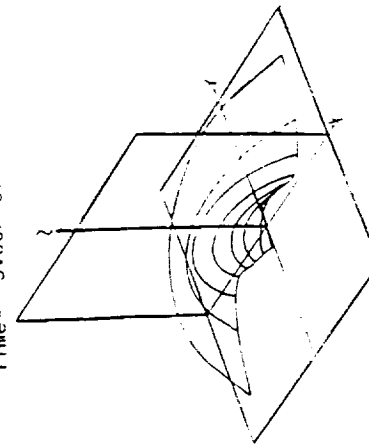


Figure 1 The evolution of magnetic arcades in three-dimensions for  $\beta = 0.1$ .

ORIGINAL PAGE IS  
OF POOR QUALITY

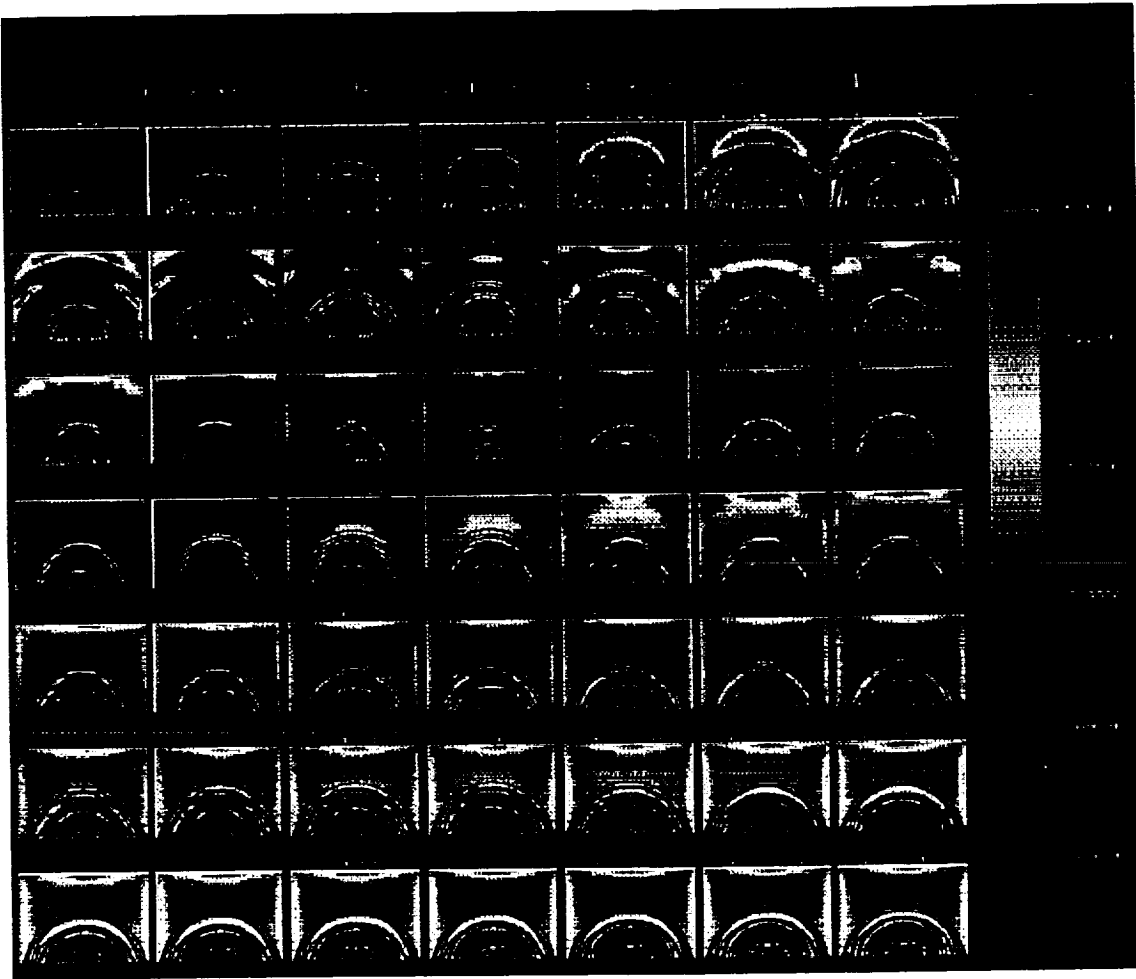


Figure 2 The evolution of density enhancement and magnetic field lines projected on the  $x - z$  plane.

numerical model. Figure 3 shows the field lines' view from the top generated by (a) analytical solutions (Low and Lou, 1990) and (b) numerical solution obtained from extrapolation. Figure 4 shows three-dimensional field lines corresponding to the solutions given in Figure 3. By observing these results, it clearly demonstrates that the PEM is a reasonable method to obtain nonlinear force-free fields by using the vector magnetograph data. The accuracy of the extrapolation can be shown as a dependence of height. It is recognized from these results that the height of the extrapolation is about one tenth of the horizontal boundary which is typically about 30,000 - 50,000 km.

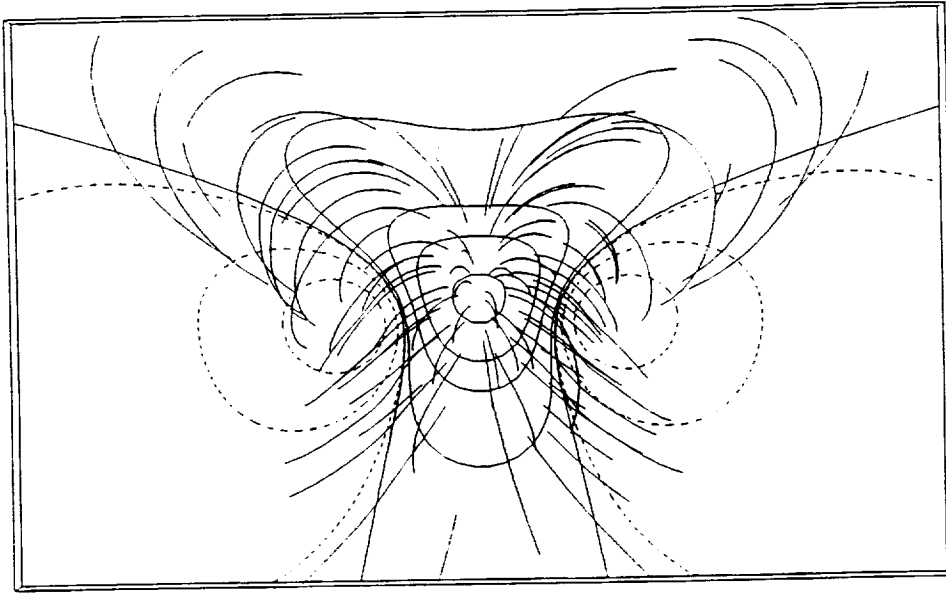
It is understood that the analytical solution is noise free. In order to show that the PEM is a viable method to analyze observed vectoral magnetograph data we have chosen the 1989 March 10 flare data for our tests. Initial results show some very encouraging signs. Since there is no analytical solution to compare with the PEM's results we shall use the potential field model for benchmark testing. Namely, we use the 1989 March 10 data to perform potential field calculations using both PEM and Schmidt's (1964) numerical code. These results are shown in Figures 5 and 6. In examining these results, we may conclude that the results obtained by PEM and Schmidt are identical. This definitely shows the accuracy of the PEM. Since the credibility of the PEM is being established, we shall compute the nonlinear force-free field configuration for the 1989 March 19 data. These are shown in Figure 7. In comparing these nonlinear force-free results with potential field results obtained by the same data, we immediately recognize different physics has been revealed by these two different models. For example, there are significant shears exhibited in the flare production region in Figure 7, but, as expected, shear cannot be accommodated in Figures 5 and 6 as the nature of the potential field model.

In summary, we feel that it is time to apply the PEM for data analysis with caution. Certainly, improvements and modifications for better accuracy will be made during these studies.

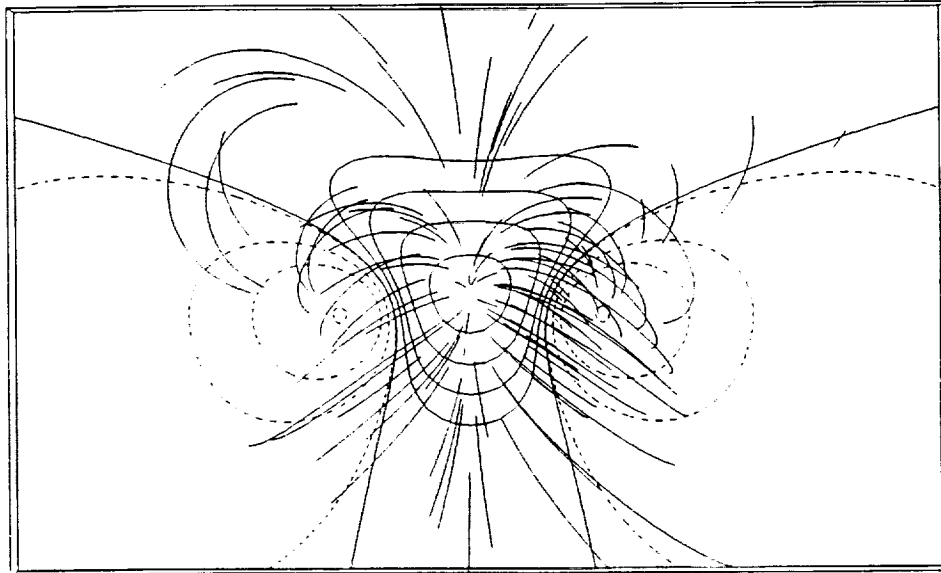
### II.3. Study of emerging flux from sub-photospheric layer

It is believed that the additional energy stored in the solar atmosphere could have resulted due to the emerging flux from the sub-photospheric layer. It is difficult to model these physics because the characteristics of this part of the solar atmosphere have several orders of magnitude variations in density, pressure and plasma  $\beta$  within a very thin layer ( $\sim 2000\text{km}$ ), hence little progress was made. In the past few months, we have been able to construct such a numerical model using the Lagrangian method. The Lagrangian method is chosen because the usual used Eulerian method cannot accommodate large gradient numerical computations.

Some results are obtained, the steady state density, temperature, pressure and plasma beta ( $\beta$ ) distributions as a function of heights (i.e. from the sun's surface up to 2000 km) are shown in Figure 8. After we obtained this steady state structured atmosphere, we introduced an emerging flux at the lower boundary and computed the evolutionary state of plasma properties. These results are shown in Figures 9, 10 and 11. These figures



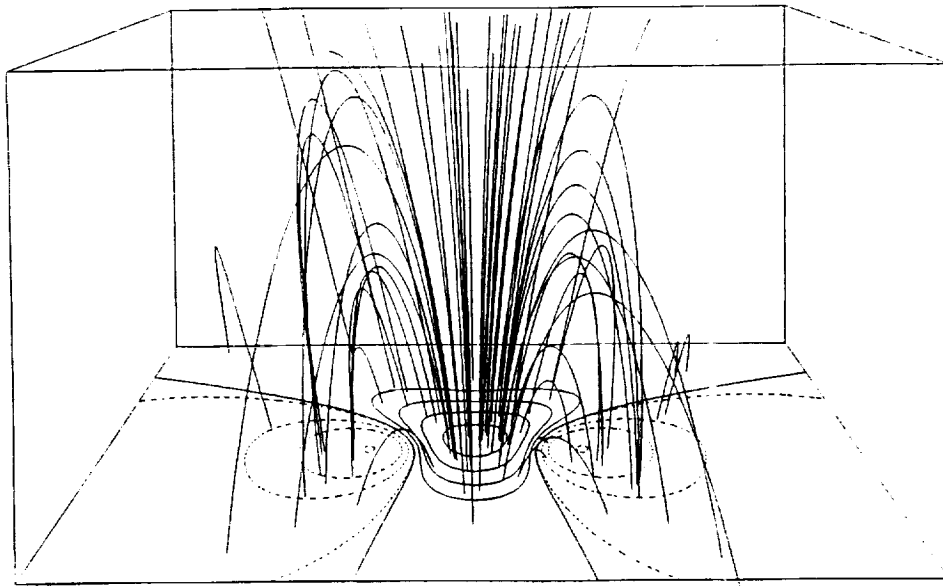
(a)



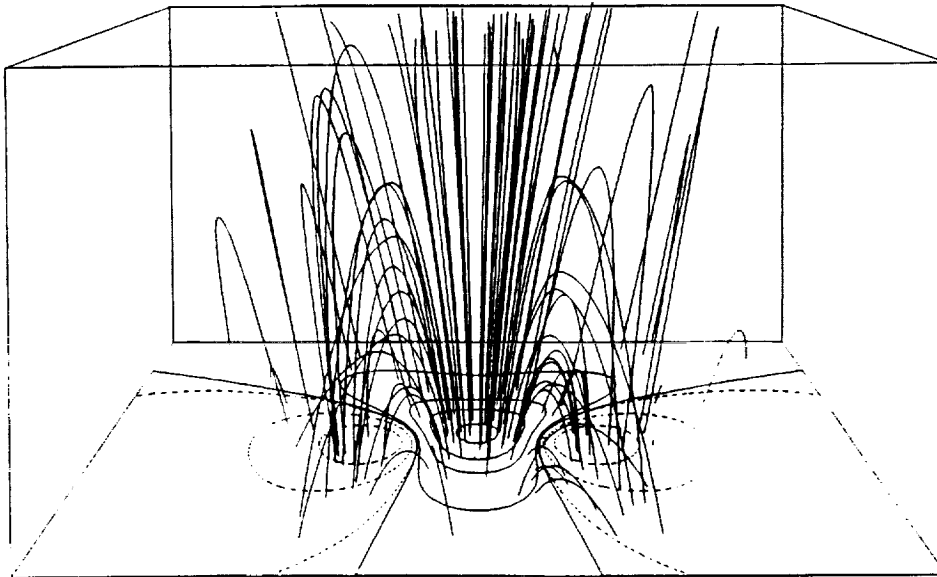
(b)

Figure 3 Comparison between the (a) analytical solution (Low and Lou, 1990) and (b) numerical solution obtained by PEM for projected magnetic field lines on  $x-y$  plane viewed from the top.



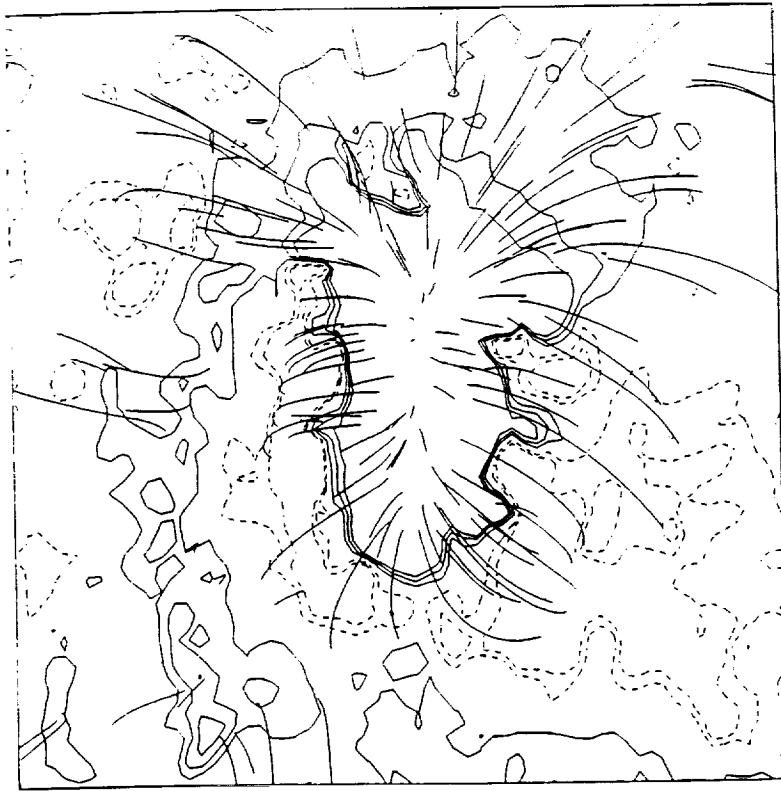


(a)

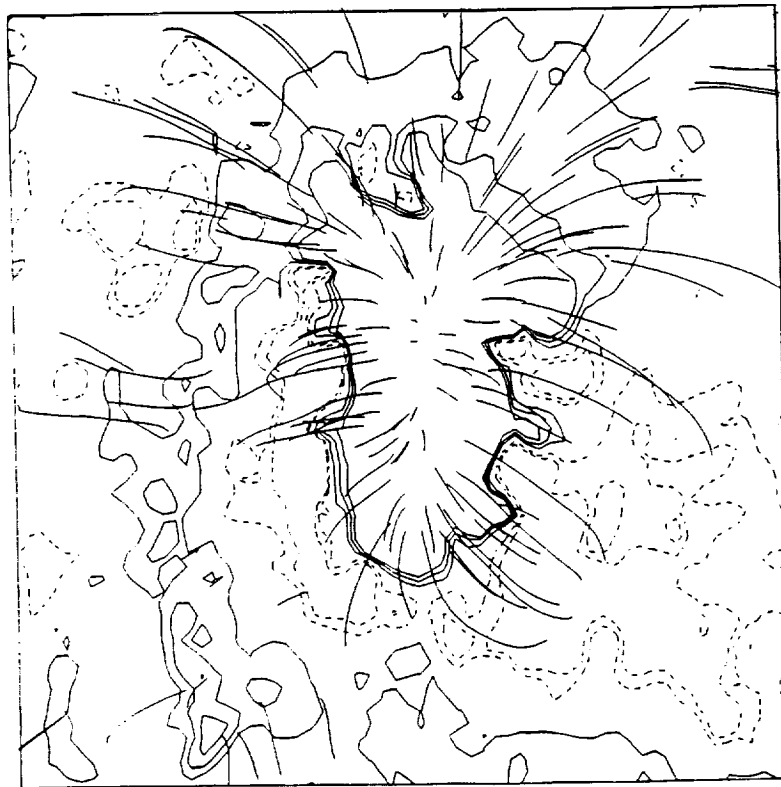


(b)

Figure 4 Comparison between (a) analytical solution (Low and Lou, 1990) and (b) numerical solution obtained by PEM for three-dimensional representation of magnetic field lines.

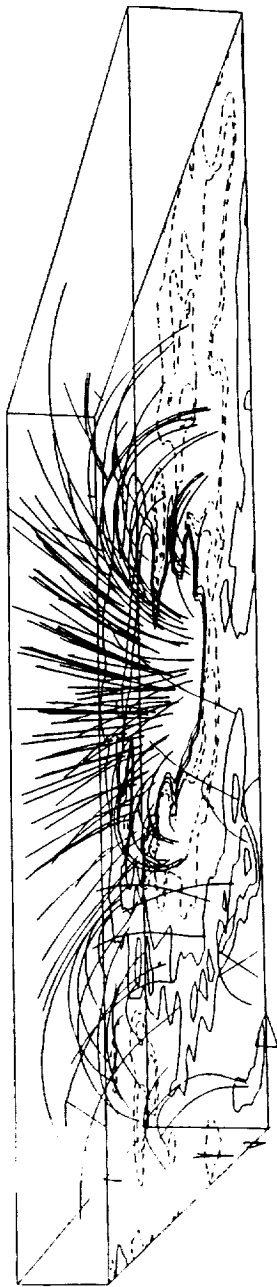


(a)



(b)

Figure 5 Comparison between the magnetic field lines projected on the solar surface ( $z = 0$ ) obtained by (a) Schmidt's potential model and (b) PEM with  $\alpha = 0$ , using 1989 March 10 magnetograph data.

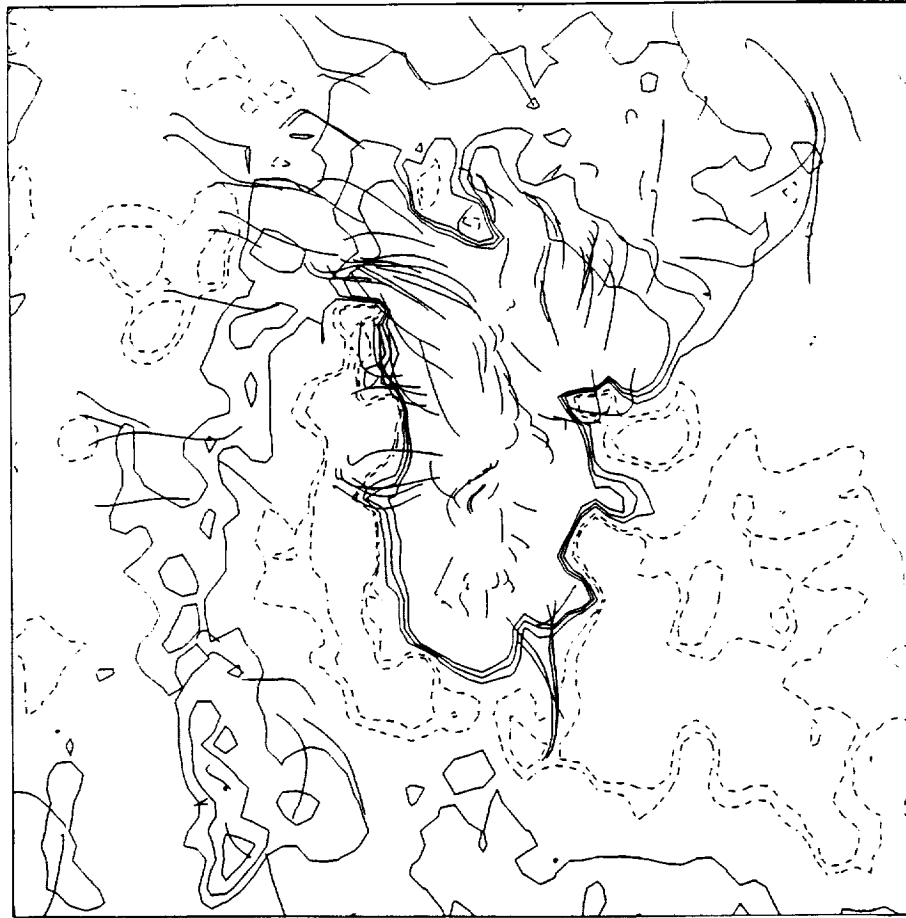


(a)



(b)

Figure 6 Comparison between the three-dimensional representation of magnetic field lines obtained by (a) Schmidt potential model and (b) PEM with  $\alpha = 0$  using 1989 March 10 magnetograph data.



nfo0310.01

0300UT

1 64

1 64

(a)



(b)

Figure 7 Computed magnetic field lines using PEM for nonlinear force-free model for the 1989 March 10 magnetograph data: (a) projected on  $z = 0$  plane and (b) three-dimensional representation.

represent the temperature, density, pressure, magnetic field lines, velocity and Lagrangian grid distribution at times, 50s, 500s, and 1050 s after introduction of the magnetic flux respectively. Presently, we are analyzing these results in detail. At first glance at these results, we could summarize our present understanding as follows:

- The emerging flux leads to the formation of a current sheet at the interface of the old and new magnetic field.
- This current sheet propagates upward.
- The induced plasma flow is oscillating at the Brunt-Vaisala frequency and has a period of 240 sec.
- Also, we show that there is no oscillation when the gravity is ignored.
- The maximum downward flow occurs in the neighborhood of legs of the magnetic loop.

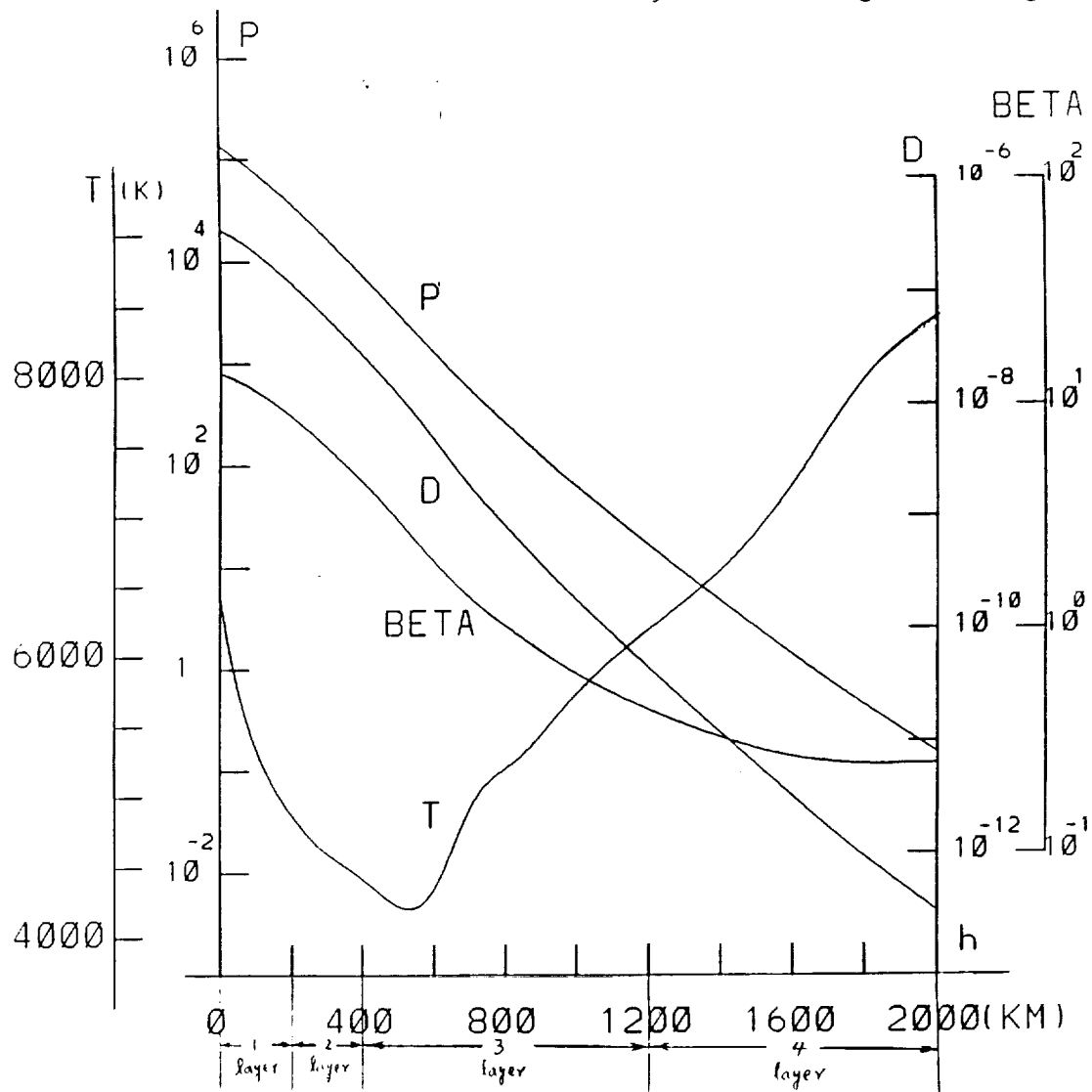
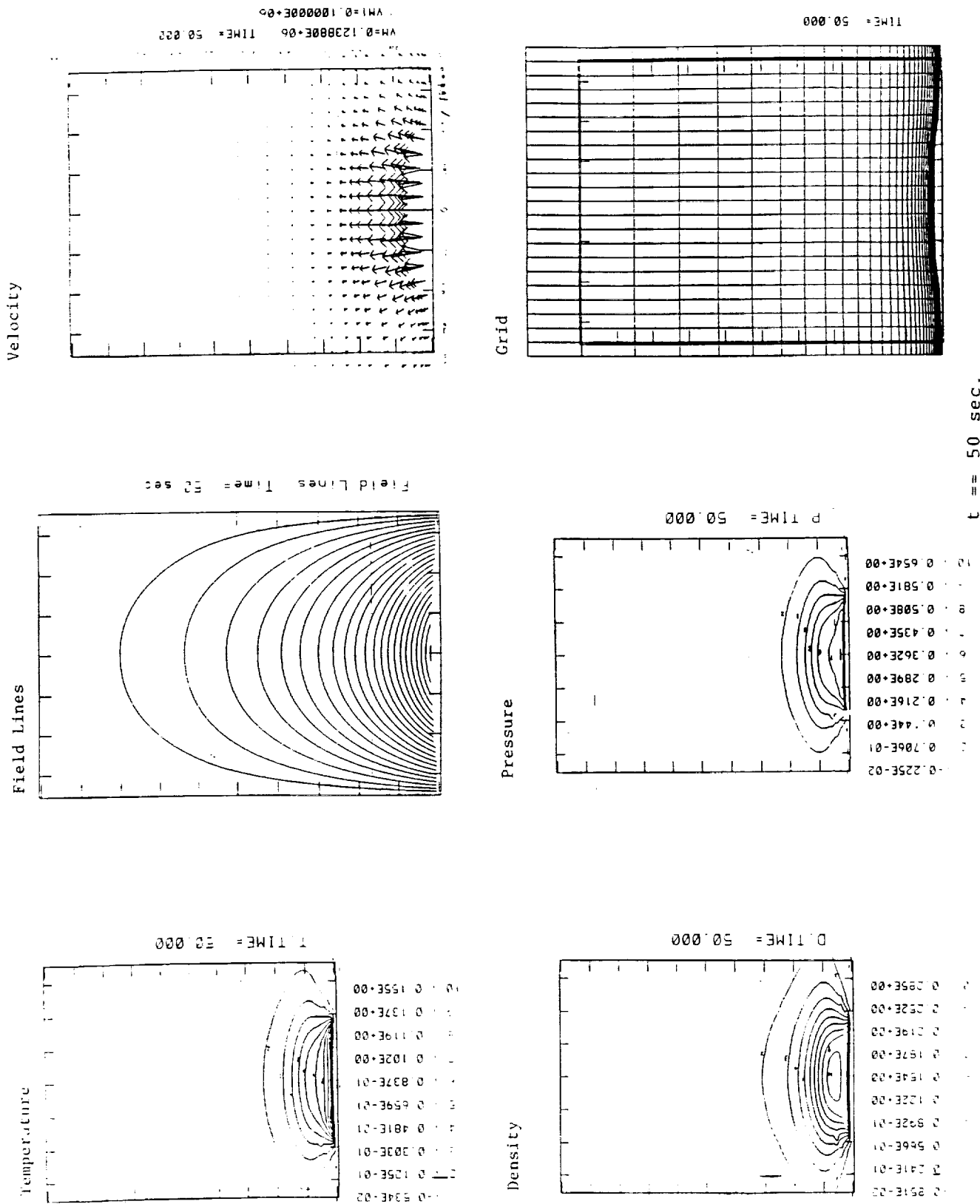


Figure 8 The distribution of density, temperature, pressure and plasma  $\beta$  as a function of height in the region of photosphere and chromosphere.



$t == 50$  sec.

Figure 9 The contours of temperature, density, pressure, magnetic field lines, velocity and Lagrangian grid distribution at 50s after introduction of energy flux.

ORIGINAL PAGE IS  
OF POOR QUALITY

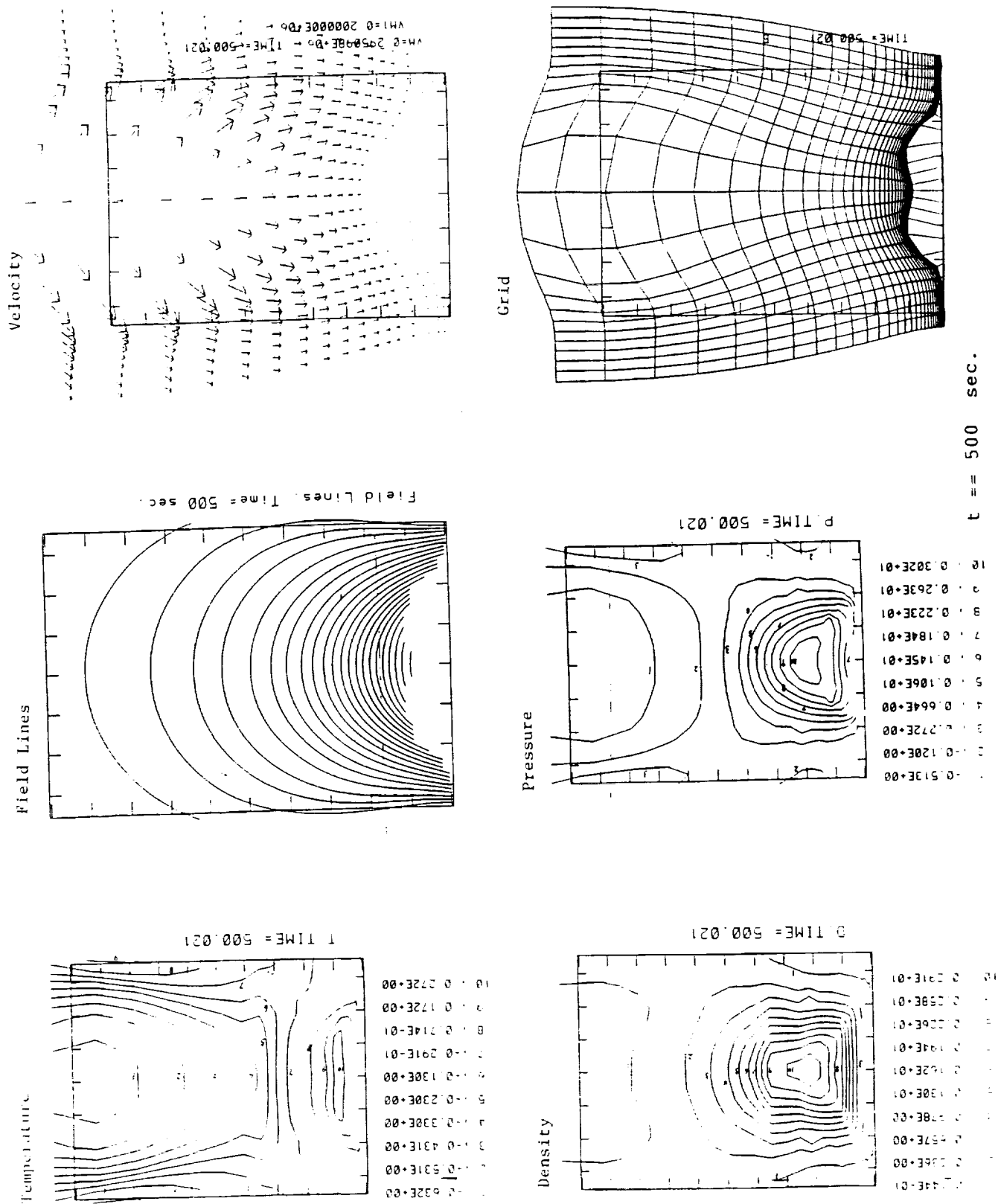
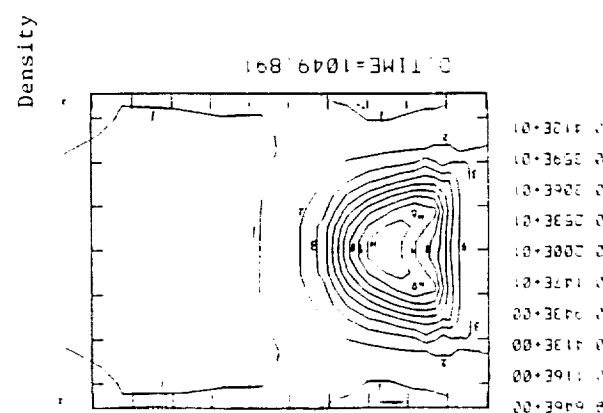
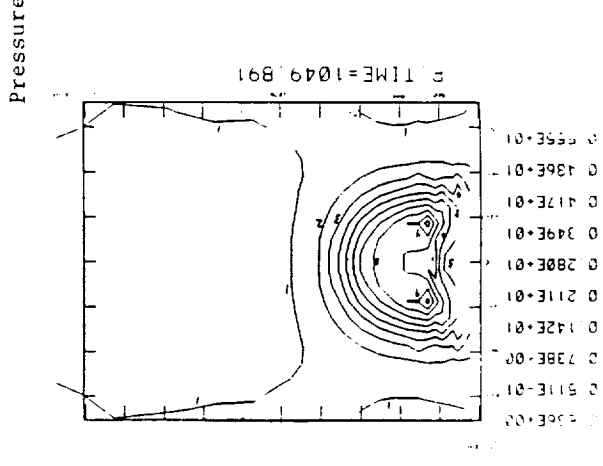
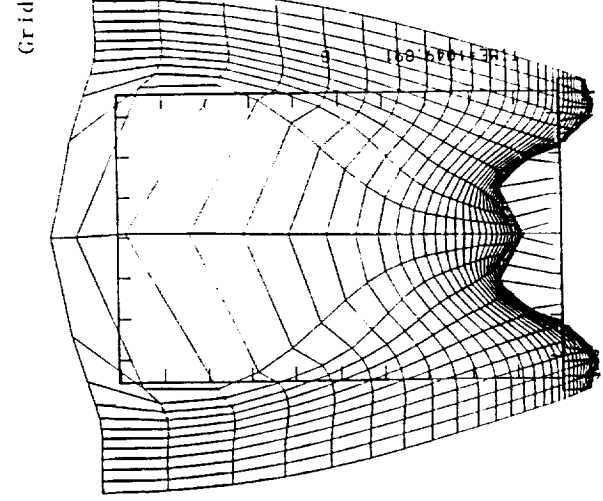
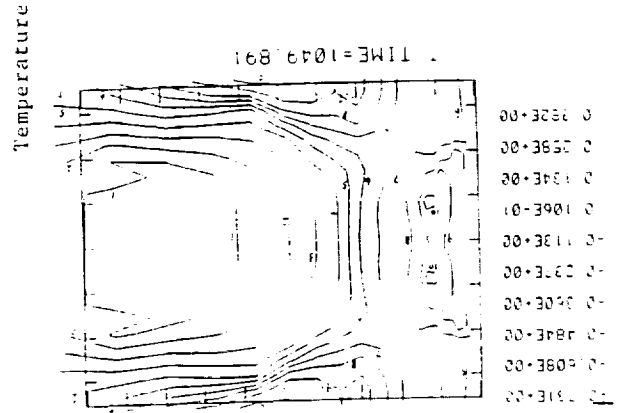
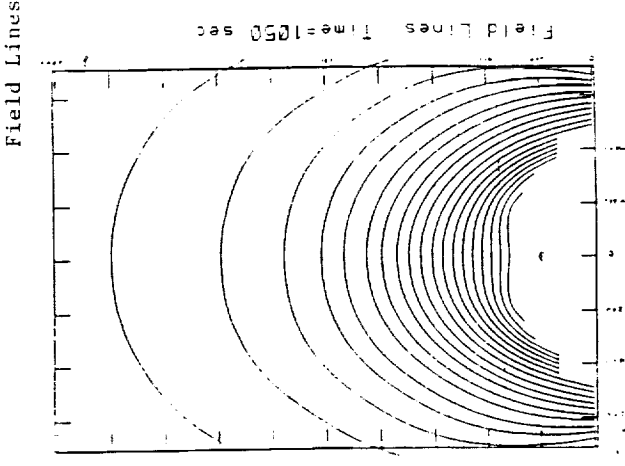
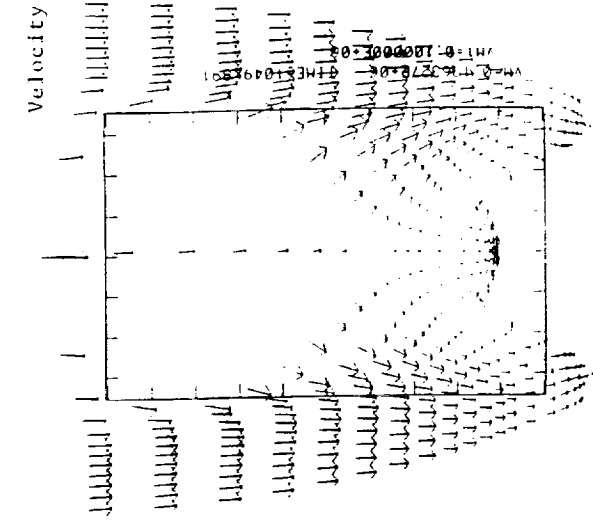


Figure 10 The contours of temperature, density, pressure, magnetic field lines, velocity and Lagrangian grid distribution at 500s after introduction of energy flux.



t == 1050 sec.

Figure 11 The contours of temperature, density, pressure, magnetic field lines, velocity and Lagrangian grid distribution at 1000s after introduction of energy flux.

ORIGINAL PAGE IS  
OF POOR QUALITY



### III. Tasks for the Third Year Grant (January 1, 1992 - December 31, 1992)

In view of the present progress, we shall continue the present course and fine tuning the present studies according to our schedule presented in the original proposal with the modification presented in January 24, 1991. Specific tasks for the coming year (Jan. 1 - Dec. 31, 1992) are:

#### III.1. Radiation and thermal conduction effects on nonlinear evolution of critical equilibria

This is the task we deleted in FY 1991 because of insufficient funding. Since the successful study described in Section II.1 in which the radiation and thermal conduction were ignored. We felt that if we wish to understand the MHD "non-equilibria" quantitatively, it is imperative to study the higher order effects on the energy transport such as radiation and thermal conduction. Thus, we propose to include this in our tasks of FY 1992.

#### III.2. Quantitative analysis of the 1989 March flares

As we discussed in Section II.2 PEM is a reasonable tool to extrapolate the realistic solar magnetic field from the photospheric level upward to the lower corona. With further development of PEM, we expect that the PEM will be able to obtain the field configuration up to 10 solar radii. Presently, we have obtained magnetic field data from Big Bear Observatory and Beijing Observatory during the flare period March 8-15, 1989. We shall use the PEM to extrapolate solar magnetic fields (see example shown in Figure 7). We expect to obtain the quantitative description of the three-dimensional flare characteristics, such as, the pre-flare and post-flare state field configurations, critical currents intensity in relation to flare onset, and amount of energy stored and released.

#### III.3. Study the energy and momentum transport from the sub- photospheric layer

Using the newly developed model described in II. 3 we will study the energy and momentum transport from the sub-photosphere upward to the corona to understand the physics of corona heating and solar wind acceleration.

#### III.4. Assessment of the three year study

We shall summarize our new findings, success, failures and the present understanding of the solar eruptive phenomena.

### References

- Low, B. C. and Y. Q. Lou, 1990. *Astrophys. J.* **352**, 343.  
Schmidt, H. U., 1964, *Physics of Solar Flares* (NASA SP-50), p. 107.  
Wu, S. T., M. T. Song, H. M. Chang, M. J. Hagyard, and G. A. Gary, 1990. *Astrophys. J.* **362**, 698.

This page left blank intentionally.

This page left blank intentionally

This page left blank intentionally.

## APPENDIX

# Performance Schedule

| TASK  | CY 1990 |   |   |   | CY 1991 |   |   |   | CY 1992 |   |   |   | CY 1993 |   |   |   |   |   |   |   |   |   |   |   |
|---|---------|---|---|---|---------|---|---|---|---------|---|---|---|---------|---|---|---|---|---|---|---|---|---|---|---|
|   | J       | F | M | A | M       | J | J | A | S       | O | N | D | J       | F | M | A | M | J | J | A | S | O | N | D |
| 1. Solar Eruptive Phenomena   | J       | F | M | A | M       | J | J | A | S       | O | N | D | J       | F | M | A | M | J | J | A | S | O | N | D |
| 1.1. Critical Shear   |         |   |   |   |         |   |   |   |         |   |   |   |         |   |   |   |   |   |   |   |   |   |   |   |
| a. Quasi-static Shear and MHD stability   |         |   |   |   |         |   |   |   |         |   |   |   |         |   |   |   |   |   |   |   |   |   |   |   |
| b. Non-linear evolution of critical equilibria  |         |   |   |   |         |   |   |   |         |   |   |   |         |   |   |   |   |   |   |   |   |   |   |   |
| 1.2. Radiation and thermal conduction effects on nonlinear evolution of critical equilibria |         |   |   |   |         |   |   |   |         |   |   |   |         |   |   |   |   |   |   |   |   |   |   |   |
| 2. Prominence Formation   |         |   |   |   |         |   |   |   |         |   |   |   |         |   |   |   |   |   |   |   |   |   |   |   |
| 2.1. Non-force-free initial B-field   |         |   |   |   |         |   |   |   |         |   |   |   |         |   |   |   |   |   |   |   |   |   |   |   |
| 2.2. Effect of shearing   |         |   |   |   |         |   |   |   |         |   |   |   |         |   |   |   |   |   |   |   |   |   |   |   |
| 2.3. Coronal cavities   |         |   |   |   |         |   |   |   |         |   |   |   |         |   |   |   |   |   |   |   |   |   |   |   |
| 3. Large Scale Global Evolution of Solar B-Field  |         |   |   |   |         |   |   |   |         |   |   |   |         |   |   |   |   |   |   |   |   |   |   |   |
| 3.1. Numerical model development  |         |   |   |   |         |   |   |   |         |   |   |   |         |   |   |   |   |   |   |   |   |   |   |   |
| 3.2. Verification of numerical models   |         |   |   |   |         |   |   |   |         |   |   |   |         |   |   |   |   |   |   |   |   |   |   |   |
| 3.3. Physical examples  |         |   |   |   |         |   |   |   |         |   |   |   |         |   |   |   |   |   |   |   |   |   |   |   |
| 3.4. Comparison with available observations   |         |   |   |   |         |   |   |   |         |   |   |   |         |   |   |   |   |   |   |   |   |   |   |   |
| 4. Overall Assessment of These Studies (i.e., 1,2,3) Based on Observations                  |         |   |   |   |         |   |   |   |         |   |   |   |         |   |   |   |   |   |   |   |   |   |   |   |



The University  
Of Alabama  
In Huntsville

College of Engineering  
Department of Mechanical Engineering  
Civil and Chemical Engineering Programs

Huntsville, Alabama 35899  
Phone: (205) 895-6154

24 January 1991

Dr. William J. Wagner  
Solar Physics Branch  
Space Physics Division  
SS  
NASA Headquarters  
Washington, DC 20546

Dear Dr. Wagner: <sup>Bill</sup>

Per your request, I am submitting the descoped tasks to be performed during the period 1 Jan 1991 - 31 Dec 1991 for proposal UAH90-309R, renewal of grant NAGW-9 in the attached sheets.

Thank you for your attention.

Sincerely,

S.T.

S. T. Wu  
Director, CSPAR  
and Distinguished Professor

Jan. 24, 1991

Tasks to be performed during the period 1 Jan 1991 - 31 Dec 1991 for the Grant NAGW-9.

1. Critical Shear Study

- (a) Employ our three-dimensional magnetohydrodynamic model to study the evolution of critical equilibria for a non-linear force-free field.
- (b) Determine the critical values of the physical parameters for the solar flare or other eruptive phenomena based on the results obtained from (a) together with the analytical model described in Section II.1 of the proposal submitted June 8, 1990.

2. Numerical Tests of the Progressive Extension Method (PEM) for the Extrapolation of Nonlinear Force-Free Field.

We plan to perform further numerical tests to establish the limits and accuracy of PEM developed by the principal investigator (Wu et al. 1990, Ap. J., 362, 698-708) for the extrapolation of nonlinear force-free magnetic fields from the solar vector magnetograph.

Additional funding of \$7,000 is requested to provide support of a student for 4 1/2 months to prepare 1989 March Flare data for analyses. We expect to employ our nonlinear force-free model to deduce the flare characteristics from 1989 March flare data which will give us the pre-flare field configuration, post-flare field configuration, critical current intensity in relation to flare onset, amount of energy released and amount of energy stored.



## ATTACHMENTS

1. S. T. Wu and Ai-Hwa Wang, "Numerical Simulation of Extended Corona", 1991, Adv. Space Res., Vol. 11, No. 1, 187.
2. Tyan Teh and S. T. Wu, "Model Calculations of the Rising Motion of a Prominence Loop", 1991, Solar Physics, 132, 335.
3. S. T. Wu, M. T. Song, P. C. H. Marten, and M. Dryer, "Shear Induced Instability and Arch Filament Eruption: A Magnetohydrodynamic (MHD) Numerical Simulation", 1991, Solar Physics, (in press).
4. S. T. Wu, M. T. Song and E. Tandberg-Hanssen, "A Numerical Simulation of Atmospheric Responses Due to Emerging Flux From Sub-Photospheric Layers", Bull. American Astronomical Society, (Abstract) Solar Physics Division Meeting, Huntsville, AL, April 1991.
5. M. T. Sun, S. T. Wu, F. S. Weng, and M. T. Song, "Further Numerical Tests for the Progressive Extension Method (PEM) for Extrapolation of Solar Force- Free Magnetic Field", Bull. American Astronomical Society, (Abstract) Solar Physics Division Meeting, Huntsville, AL, April 1991.

# NUMERICAL SIMULATION OF EXTENDED CORONA

S. T. Wu and Ai-Hwa Wang

*Center for Space Plasma and Aeronomic Research and Department of Mechanical Engineering, The University of Alabama in Huntsville, Huntsville, AL 35899, U.S.A.*

## ABSTRACT

A three-dimensional, time-dependent magnetohydrodynamic (MHD) model is presented for the study of coronal dynamics. The model, written in spherical coordinates, extends from the solar surface ( $1R_s$ , where  $1R_s = 6.95 \times 10^5$  km) to  $15 R_s$ . This model was developed with two major issues in mind, namely for interpretation of various steady state and evolutionary dynamical structures in the corona. In order to achieve these objectives we have employed two different numerical techniques to seek solutions for these two different, but related, problems; steady state structures and evolutionary structures. These two numerical techniques are: (i) relaxation technique for steady state structures; and (ii) FICE (Full-Implicit-Continuous-Eulerian) technique for evolutionary structures.

To illustrate this model, we present numerical results for examples of both the steady state and evolutionary structure of the corona. These results show the additional physical features which cannot be shown by a two-dimensional model. Finally, on the basis of the exploratory calculation, we outline some interesting physical features which can be considered for the observing programs of future space missions such as SOHO, OSL, CORONAS, etc.

## I. INTRODUCTION

Since the Skylab-ATM experiments in the seventies, we have recognized that the corona is in a transient state in contrast to the previous understanding whereby the corona is always in a quiet orderly state (Billings, 1966). It is also further realized that the relationship between the flare and the coronal mass ejection is not as consistently intimate as originally thought (Hildner et al. 1976). In order to understand the physics of this fascinating phenomena of so-called "coronal transients", a number of theoretical models has been presented in the literature (Hundhausen et al. 1984). All of these theoretical models are based on magnetohydrodynamic theory. The methodology used to treat these theoretical models could be classified into two categories: (i) analytical methods and (ii) numerical methods. Those models treated by analytical methods have to conform to certain strict conditions in which a full description of nonlinear dynamical behavior is difficult to achieve; nevertheless, the solutions are exact. On the other hand, the models treated by numerical methods could obtain global descriptions of nonlinear dynamics, but these descriptions are not unambiguous and may mislead the physical interpretations. A further limitation to these two categories is the fact that all of these models are confined to a two-dimensional geometry. Thus, it is inevitable that some arguments in the interpretation of observations have taken place.

In this paper, we present a newly developed *three-dimensional*, time-dependent, magnetohydrodynamic model for an extended corona. We will suggest that this model could be used to understand the physical processes from the comparison of this model's results with observational data. The theoretical description of the model presents the basis for the addition of dissipative mathematical terms that could be used to understand additional physical processes from specific observational data. The theoretical description of the model are included in Section II. The numerical results are presented in Section III. Finally, the concluding remarks are included in Section IV.

## II. ANALYSES

### Mathematical Model

In this study, we have assumed that the solar atmosphere behaves as a single fluid with negligible dissipative effects. With these assumptions, the time-dependent magnetohydrodynamic (MHD) equations that describe

atmospheric flows in three-dimensions for a spherical coordinate system can be written as follows:

$$\frac{\partial \rho}{\partial t} = -\frac{1}{r^2} \frac{\partial(r^2 \rho v_r)}{\partial r} - \frac{1}{r \sin \theta} \frac{\partial(\rho v_\theta \sin \theta)}{\partial \theta} - \frac{1}{r \sin \theta} \frac{\partial(\rho v_\phi)}{\partial \phi} \quad (1)$$

$$\begin{aligned} \frac{\partial v_r}{\partial t} = & -v_r \frac{\partial v_r}{\partial r} - \frac{v_\theta}{r} \frac{\partial v_r}{\partial \theta} - \frac{v_\phi}{r \sin \theta} \frac{\partial v_r}{\partial \phi} - \frac{1}{\rho} \left[ \frac{\partial(\rho RT)}{\partial r} + B_\theta \left( \frac{\partial B_\theta}{\partial r} - \frac{1}{r} \frac{\partial B_r}{\partial \theta} \right) \right. \\ & \left. - B_\phi \left( \frac{1}{r \sin \theta} \frac{\partial B_r}{\partial \phi} - \frac{\partial B_\phi}{\partial r} \right) \right] + \frac{v_\phi^2 + v_\theta^2}{r} - \frac{B_\phi^2 + B_\theta^2}{\rho r} - \frac{GM}{r^2} \end{aligned} \quad (2)$$

$$\begin{aligned} \frac{\partial v_\theta}{\partial t} = & -v_r \frac{\partial v_\theta}{\partial r} - \frac{v_\theta}{r} \frac{\partial v_\theta}{\partial \theta} - \frac{v_\phi}{r \sin \theta} \frac{\partial v_\theta}{\partial \phi} - \frac{1}{\rho} \left[ \frac{\partial(\rho RT)}{r \partial \theta} - B_r \left( \frac{\partial B_\theta}{\partial r} - \frac{1}{r} \frac{\partial B_r}{\partial \theta} \right) \right. \\ & \left. - B_\phi \left( \frac{1}{r \sin \theta} \frac{\partial B_\theta}{\partial \phi} - \frac{\partial B_\phi}{r \partial \theta} \right) \right] - \frac{v_r v_\theta - v_\phi^2 \cot \theta}{r} - \frac{B_r B_\theta - B_\phi^2 \cot \theta}{\rho r} \end{aligned} \quad (3)$$

$$\begin{aligned} \frac{\partial v_\phi}{\partial t} = & -v_r \frac{\partial v_\phi}{\partial r} - \frac{v_\theta}{r} \frac{\partial v_\phi}{\partial \theta} - \frac{v_\phi}{r \sin \theta} \frac{\partial v_\phi}{\partial \phi} + \frac{B_r}{\rho} \frac{\partial B_\phi}{\partial r} - \frac{B_\theta}{r} \frac{\partial B_\phi}{\partial \theta} - \frac{1}{r \rho \sin \theta} \\ & \left( \frac{\partial(\rho RT)}{\partial \phi} + B_r \frac{\partial B_r}{\partial \phi} + B_\theta \frac{\partial B_\theta}{\partial \phi} \right) + \frac{B_\phi}{\rho r} (B_r + B_\theta \cot \theta) - \frac{v_\phi}{r} (v_r + v_\theta \cot \theta) \end{aligned} \quad (4)$$

$$\frac{\partial B_r}{\partial t} = \frac{1}{r \sin \theta} \left[ \frac{\partial}{\partial \theta} (\sin \theta (v_r B_\theta - v_\theta B_r)) - \frac{\partial}{\partial \phi} (v_\phi B_r - v_r B_\phi) \right] \quad (5)$$

$$\frac{\partial B_\theta}{\partial t} = \frac{1}{r \sin \theta} \frac{\partial}{\partial \phi} (v_\theta B_\phi - v_\phi B_\theta) - \frac{1}{r} \frac{\partial}{\partial r} [r (v_r B_\theta - v_\theta B_r)] \quad (6)$$

$$\frac{\partial B_\phi}{\partial t} = \frac{1}{r} \frac{\partial}{\partial r} [r (v_\phi B_r - v_r B_\phi)] - \frac{1}{r} \frac{\partial}{\partial \theta} (v_\theta B_\phi - v_\phi B_\theta) \quad (7)$$

$$\begin{aligned} \frac{\partial T}{\partial t} = & -(\gamma - 1) T \left[ \frac{1}{r^2} \frac{\partial(r^2 v_r)}{\partial r} + \frac{1}{r \sin \theta} \frac{\partial(v_\theta \sin \theta)}{\partial \theta} + \frac{1}{r \sin \theta} \frac{\partial v_\phi}{\partial \phi} \right] \\ & - v_r \frac{\partial T}{\partial r} - \frac{v_\theta}{r} \frac{\partial T}{\partial \theta} - \frac{v_\phi}{r \sin \theta} \frac{\partial T}{\partial \phi} \end{aligned} \quad (8)$$

where the dependent variables are the density  $\rho$ , temperature  $T$ , velocity  $(v_r, v_\theta, v_\phi)$ , and magnetic field  $(B_r, B_\theta, B_\phi)$ . The independent variables are the radius  $r$ , the meridional angle  $\theta$  and azimuthal angle  $\phi$  as well at time "t". The constants are the polytropic index  $\gamma$ , solar total mass  $M$  and gravitational constant  $G$ . In addition, the standard equation of state ( $p = \rho RT$ ) was used to obtain the above set of governing equations.

The region, within which we will present the numerical solution to the above set of governing equations, is shown in Figure 1. This region is bounded by the solar surface and 15 solar radii ( $R_s$ ) in radial distance, by the equator and the pole in meridional distance ( $\theta$ -coordinate), and by azimuthal extent ( $\phi$ -coordinate) of  $45^\circ$ .

### Method of Solution

The equations are solved numerically using a modified FICE (Full-Implicit-Continuous-Eulerian) scheme which is based on the original FICE scheme developed by Hu and Wu (1984); and Wu and Wang (1987). The grid spacings used are  $\delta r_i = R_s(1 + \delta\theta)^{i-1}$ , and  $\delta\theta = \delta\phi = 4.5^\circ$ . It should be noted that the radial spacing is not uniform and is chosen so as to; (1) assure the initial state as being in isothermal and hydrostatic equilibrium (Wang et al. 1982); (2) initialization of the computation procedure; and (3) to ensure numerical accuracy. The time step can be arbitrarily chosen because of the flexibility of the FICE scheme.

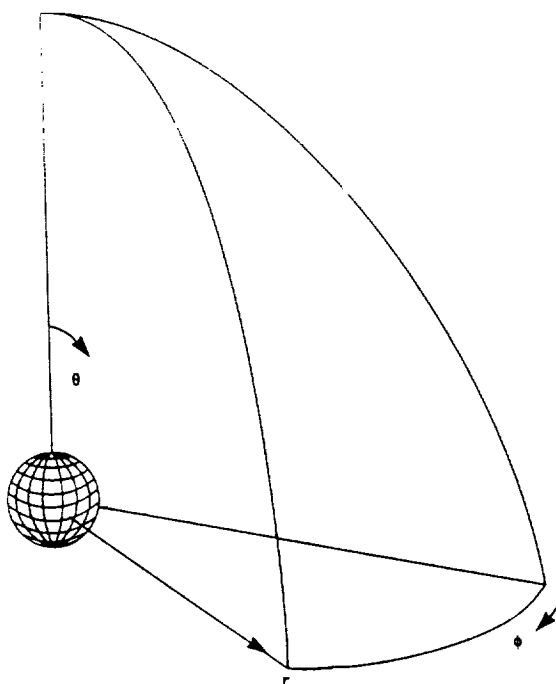


Fig. 1. A schematic description of the portion of a three- dimensional configuration in which the solution is calculated. Note that the computational domain extends from the pole to the equator within a  $45^\circ$  extent of heliographic longitude. In the present paper, symmetry is assumed below the solar equatorial plane.

### Initial State and Boundary Conditions

In order to seek a solution of this problem, we need to specify the initial conditions. These initial conditions include the magnetic field configuration, velocity field and corresponding thermodynamic properties of the plasma.

The boundary conditions are rather complicated, hence a detailed account of the derivation of the boundary conditions will be presented later (Wang and Wu, 1990). We shall only briefly describe these boundary conditions here. There are a total of six sides in which the boundary conditions need to be specified; they are:

- (1)  $r = R_s$ , eight compatibility conditions are obtained from the set of governing equations (Wu and Wang, 1987);
- (2)  $r = 15R_s$ , non-reflecting boundary conditions are used (Hu and Wu, 1984);
- (3)  $\theta = 0$  (pole) and  $\theta = 90^\circ$  (equator), symmetric conditions are chosen because of the chosen field configuration;
- (4)  $\phi = 0$  and  $\phi = 45^\circ$ , the boundary conditions are obtained by extrapolation techniques.

### III. NUMERICAL RESULTS

In order to carry out this simulation, we first introduced an initial state at isothermal and hydrostatic equilibrium with  $\gamma = 1.67$  together with a potential field in one case and, in a separate case, a linear force-free magnetic field topology. These two separate cases were introduced into the set of governing equations in order to ensure that the isothermal and hydrostatic equilibrium does exist. We then introduced a steady-state, Parker-type, velocity field. The numerical solution of this mathematical system led to a magnetohydrodynamic equilibrium state via the relaxation technique. This MHD equilibrium state is then taken as the simulated undisturbed coronal (i.e., quiet corona) with an outflowing solar wind around multiple helmet magnetic topologies.

The initial plasma and fields (magnetic and velocity) parameters incorporated in this simulation are the following representative conditions of a non-rotating sun with an initial plasma  $\beta_0 (= 16\pi n_0 k_0 T_0 / B_0^2)$  being unity, at  $r = R_s$ ,  $\theta = 90^\circ$  and  $\phi = 22.5^\circ$ .

- Isothermal and hydrostatic equilibrium atmosphere.

$$T_0 = 10^6 \text{ K}$$

$$\rho_0 = \rho_0^j \exp\left(\left(\frac{1}{R_{\text{eff}}} - 1\right) \frac{R_{\text{eff}} g_0}{RT_0}\right)$$

where  $\rho_0^j$  is the density (the value of  $1.67 \times 10^{-16} \text{ gm cm}^{-3}$  is used in this study and  $g_0$  is the gravity on the solar surface.

- Magnetic field configuration
  - (i) A hexapole potential field (Jackson, 1962); and, in a separate calculation,
  - (ii) A hexapole linear force-free field (Nakagawa et al., 1978)
- Velocity Field
 
$$v_r(1, \theta, \phi) = 15 \text{ km s}^{-1},$$

$$v_r(15, \theta, \phi) = 200 \text{ km s}^{-1},$$

$$v_\theta(r, \theta, \phi) = v_\phi(r, \theta, \phi) = 0.$$

Figure 2 shows the simulated morphology of the quiet corona which consists of a three-dimensional representation of the brightness (integrated density along the path of the line-of-sight), steady state solar wind velocity vectors and magnetic field for two cases: (a) initially potential field topology; and (b) initially linear force-free field topology, respectively. It is easy to recognize that the shape of the quiet corona depends on the initial magnetic field topology. The bright corona is related to the closed magnetic field configuration, and the dark region corresponds to the open field configuration which corresponds to the out-flowing solar wind from the coronal hole. Also it shows that the solar wind velocity is almost radial.

In order to examine the physical structure of the quiet, steady-state, corona, we plot the radial distribution of the density and temperature at the pole and equator for the initially potential and linear force-free magnetic field topologies, respectively, as shown in Figure 3. The radial distribution of the three velocity components (i.e.,  $v_r$ ,  $v_\theta$ ,  $v_\phi$ ) at the pole and equator is shown in Figure 4 for both types of magnetic field topology. Finally, we plot the radial distribution of Alfvén and sonic speed at the pole and equator in Figure 5.

Comparison of each of these parameters demonstrates the well-known inference and important fact that the magnetic field is the dominant factor that determines both the morphology and physical structure of the corona. The spatial diversity of these important, fundamental steady-state parameters is obvious.

For the completeness of this presentation, we shall show some results for a disturbed corona in Figure 6. This numerical result is obtained by introducing a pressure pulse ( $p/p_0 = 10$ ) distributed over three grid points centered at  $\theta = 35^\circ$ ,  $\phi = 22.5^\circ$  and  $r = R$ , for the case of the initially linear force-free magnetic field topology of the quiet corona as shown in Figure 2b. In Figure 6, at  $t = 600 \text{ s}$ , we show simulated brightness (i.e. line-of-sight integrated density enhancement), disturbed magnetic field and solar wind velocity vectors in the  $\phi = 22^\circ$  plane. According to the results shown, we may interpret that the brightness was caused by the flow interaction with the magnetic field. This density enhancement consists of both the mass carried by plasma flow motion and local wave compression.

#### IV. CONCLUDING REMARKS

In this study, we have presented a newly-developed, three-dimensional, time-dependent magnetohydrodynamic model for the study of corona structures in both quiet and disturbed states. This model extends from the solar surface to  $15 R$ , and, thereby, includes the region of outflowing solar wind from the subsonic, sub-Alfvénic to super-sonic and super-Alfvénic regions. Therefore, we assert that it is, indeed, a model which could be used to study coronal/interplanetary coupling problems.

In these preliminary results, we clearly recognize that the magnetic field topology and strength controls both the structures and physical parameters' morphology of the corona. Also, this model has the capability to convert the fundamental physical parameters (i.e.  $\rho$ ,  $T$ ,  $v$ ) to observables such as brightness (see Fig. 2) and doppler shifts (not shown). Therefore, we may claim that this model has the potential whereby it could be used as a diagnostic tool that can be applied to the interpretation and guidance of the observations. For example, we may use the physical properties obtained from this model to compute line profiles. As a final

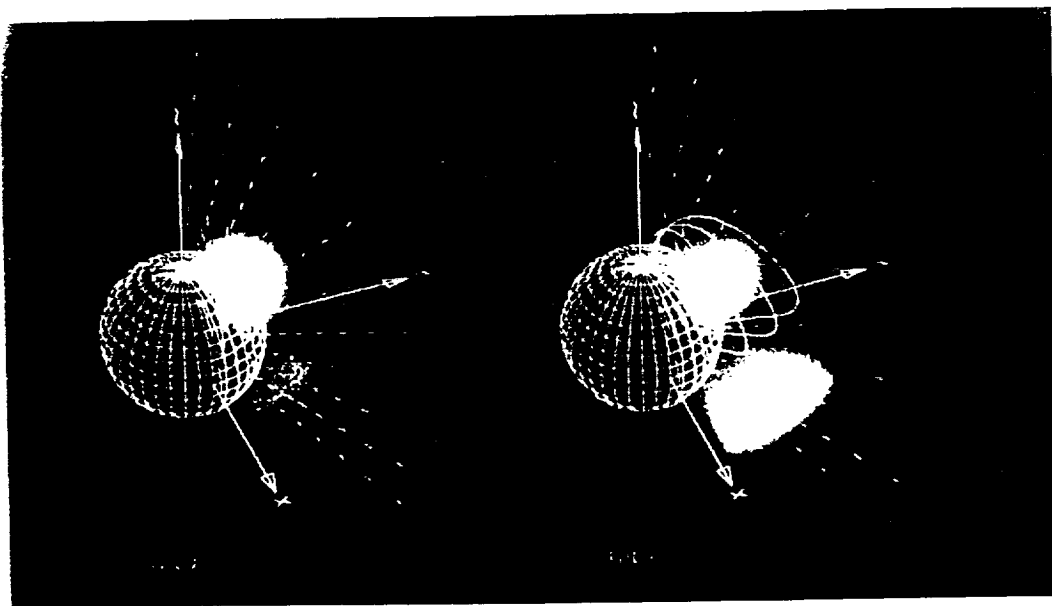


Fig. 1. The three-dimensional simulated brightness, steady state solar wind velocity vectors and magnetic field of the confined plasma corona for: (a) initially potential field configuration (upper left panel) and (b) initially linear force-free field configuration (upper right panel).

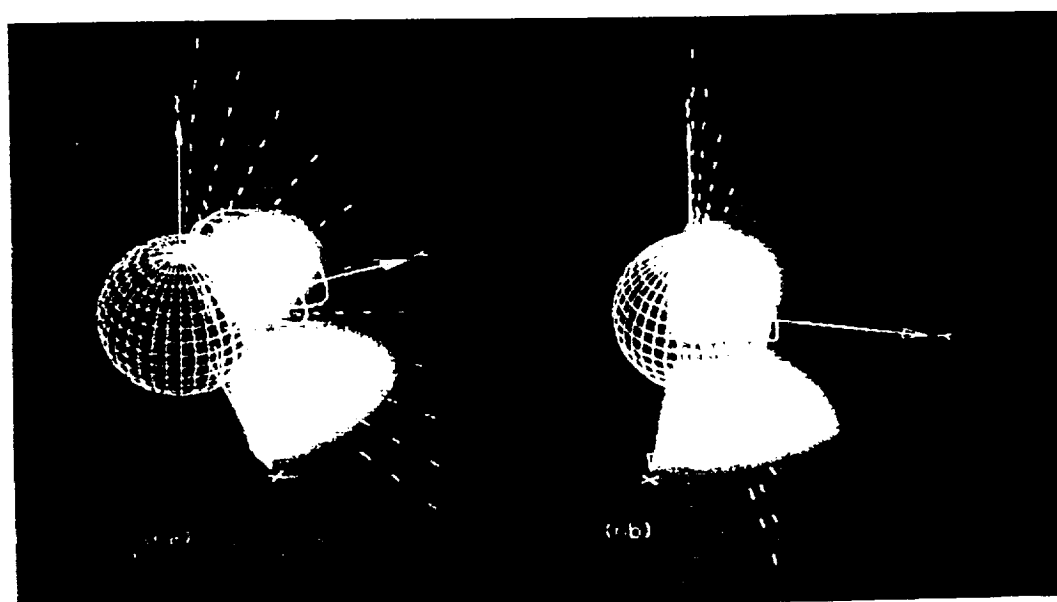


Fig. 2. The three-dimensional simulated brightness, magnetic field and solar wind velocity of a disturbed corona at 500 s after introduction of a pressure pulse (simulated flare) at solar surface of the quiet corona given in Figure 1b. (a) Viewed from  $\theta = 50^\circ$ ,  $\phi = -20^\circ$ , and (b) viewed from  $\theta = 50^\circ$ ,  $\phi = 0^\circ$ .

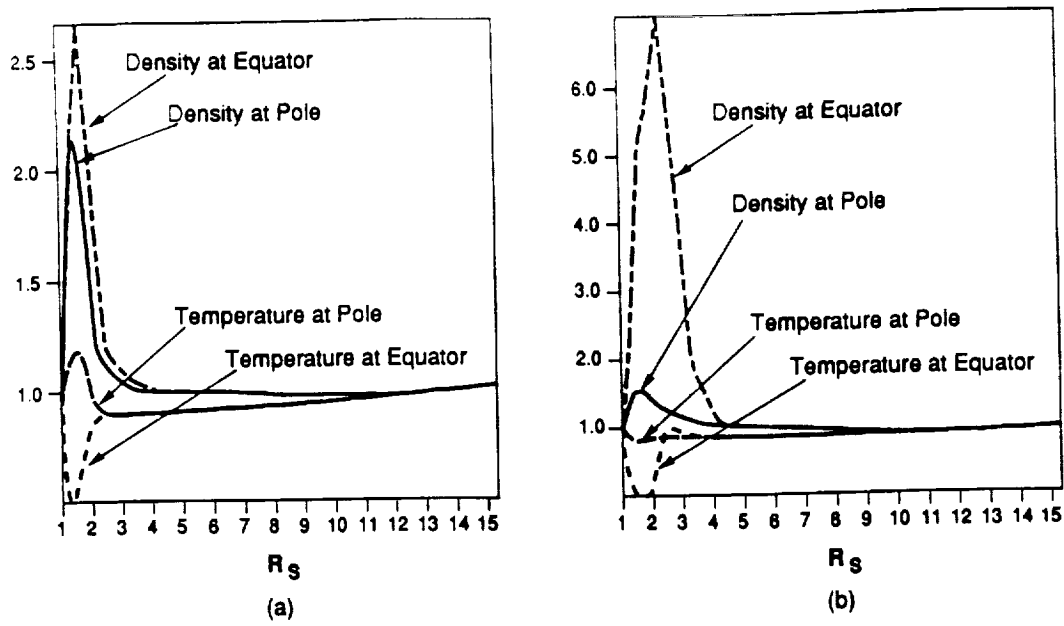


Fig. 3. Radial distribution of the density ( $\rho/\rho_0$ ) and temperature ( $T/T_0$ ) at the pole and the equator, respectively for; (a) initially potential field configuration and (b) initially linear force-free field configuration with  $\rho_0$  and  $T_0$  given in page 6 of the text.

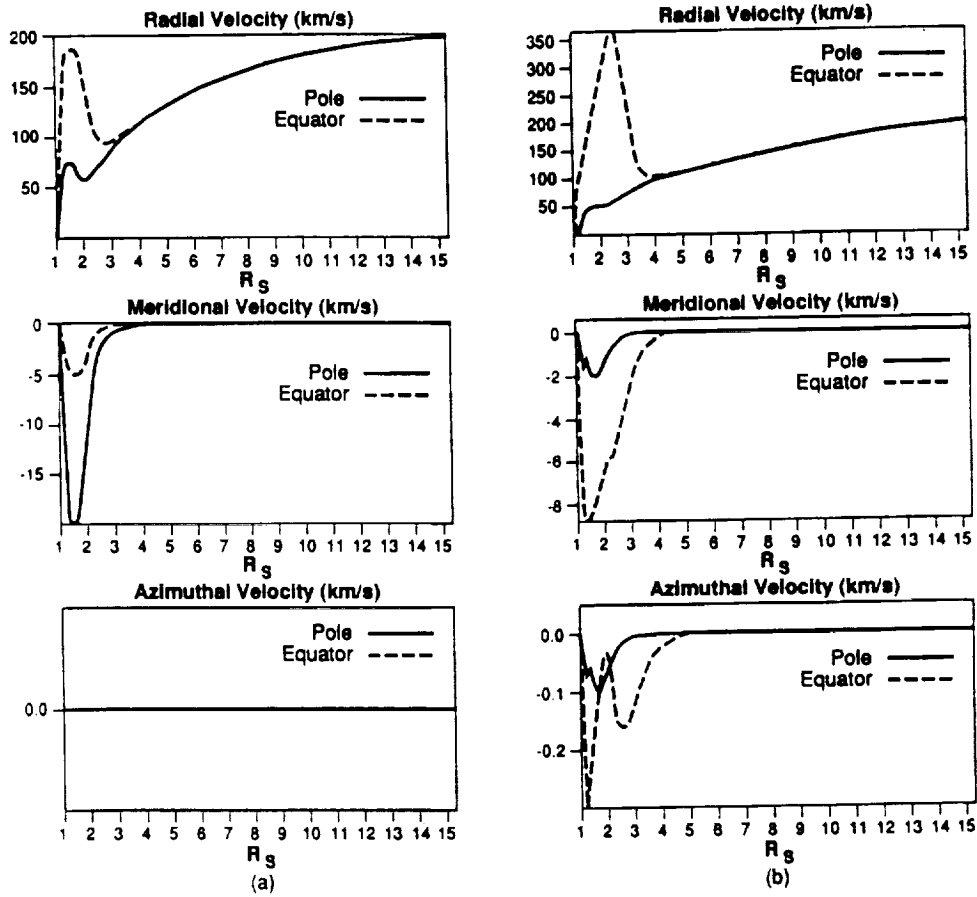


Fig. 4. Radial distribution of the three velocity components ( $v_r$ ,  $v_\theta$ ,  $v_\phi$ ) at the pole and equator for; (a) initially potential field configuration and (b) initially linear force-free field configuration.

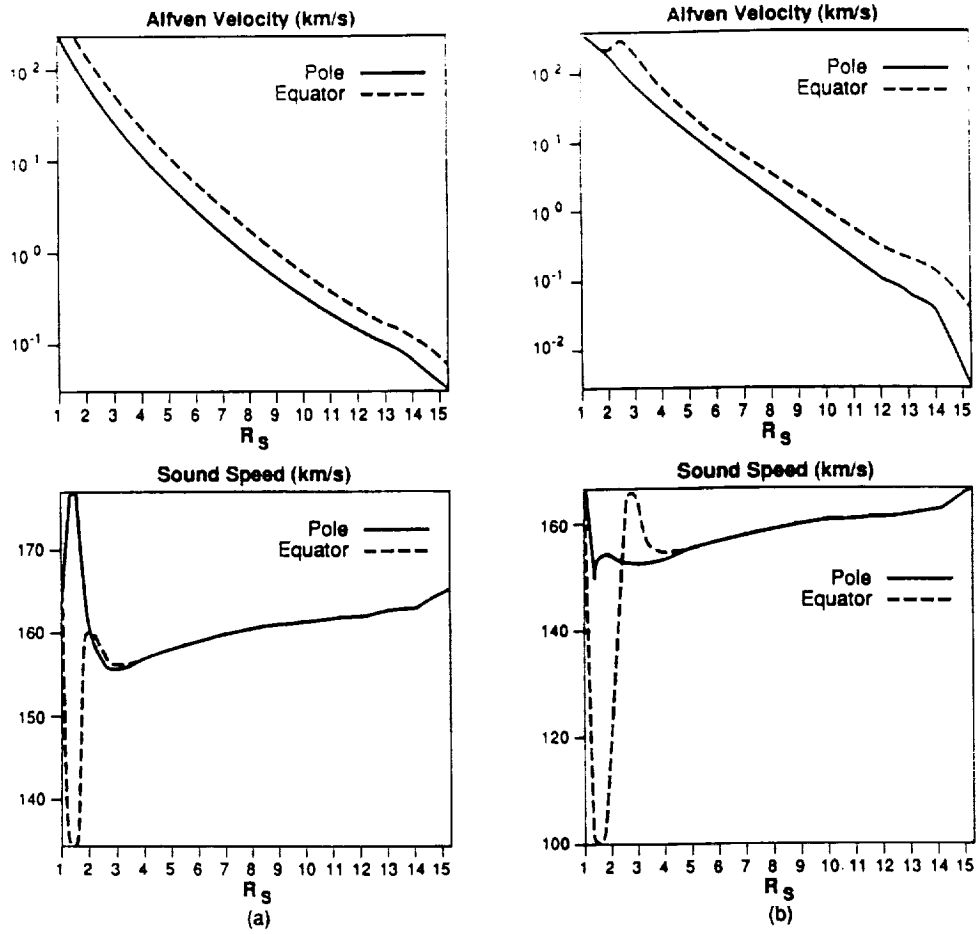


Fig. 5. Alfvénic speed and sonic speed as function of radial distance at pole and equator for (a) initially potential field configuration and (b) initially linear force-free field configuration.

remark, we recognize that the development of this model is far from complete. The improvements can be tackled in two major categories as follows:

- Mathematical Improvement

We should establish the accuracy of the numerical results. In order to achieve this purpose, we should conduct a grid size test for this model.

- Physical Improvement

Presently, the model includes dissipative mechanisms that were not invoked for the present demonstration of its three-dimensional, temporal capability. Namely, the present model results are based on "ideal" MHD theory. We realize that dissipative MHD is important to many solar physics problems in which finite electrical conductivity, thermal conductivity, radiation and turbulence are undoubtedly present. We plan to incorporate these effects in our model via a conservative and rational step-by-step approach. However, the current ideal MHD model, because of its inherent and natural three-dimensional resemblance to the real world, is essential for the construction of solutions which resemble observed realistic topologies. We have obtained in the present demonstration, for example, induced meridional and aximuthal flows which existing two-dimensional models cannot provide.

#### ACKNOWLEDGEMENT

We are indebted to Dr. Murray Dryer for reading this manuscript and making invaluable suggestions and M. T. Sun for preparing the three-dimensional color graphics. This work is supported by AFOSR-88-0013, NAGW-9 and NOAA (50RANR000104).



## REFERENCES

- Billings, D. E., 1966, *A Guide to the Solar Corona*, Academic Press, New York
- Jackson, John David, 1962, *Classical Electrodynamics*, John Wiley and Sons, Inc., New York,-London-Sydney
- Hildner, E., Gosling, J. T., MacQueen, R. M., Munro, R. H., Poland, A. I. and Ross, C. L., 1976, *Solar Physics*, **48**, 127.
- Hu, Y. Q. and Wu, S. T., 1984, *J. Comp. Phys*, **55**, 33.
- Hundhausen, A. J., Burlaga, L. F., Feldman, W. C., Gosling, J. T., Hildner, E., House, L. L., Howard, R. A., Krieger, A. S., Kundu, M. R., Low, B. C., Sheeley, N. R., Jr., Steinolfson, R. S., Stewart, R. T., Stone, R. G. and Wu, S. T., 1984, *Solar Terrestrial Physics: Present and Future*, (Butler, D. M. and Papadopoulos, K., eds) **NASA Reference Publication 1120**, Chapter 6.
- Nakagawa, Y., Wu, S. T., and Tandberg-Hanssen, E., 1978, *Astron. Astrophys.* **69**, 43.
- Wang, A. H., and Wu, S. T., 1990, *J. Comp. Phys.* (to be submitted).
- Wang, S., Hu, Y. Q. and Wu, S. T., 1982, *Scientia Sinica (Series A)* , **XXV**, 1305.
- Wu, S. T., and Wang, J. F., 1987, *Comp. Meth. in Applied Mechanics and Engineering*, **64**, 267.

# MODEL CALCULATIONS OF THE RISING MOTION OF A PROMINENCE LOOP

TYAN YEH

*Space Environment Laboratory, NOAA Environmental Research Laboratories, Boulder, CO 80303, U.S.A.*

and

S. T. WU

*Center for Space Plasma and Aeronomic Research, The University of Alabama in Huntsville, Huntsville, AL 35899, U.S.A.*

(Received 26 June, 1990; in revised form 23 October, 1990)

**Abstract.** Model calculations are presented for the rising motion of the top section of a prominence loop, which is represented by a straight flux rope immersed in a coronal medium permeated with a bipolar magnetic field. Initially the prominence is at rest, in equilibrium with the surrounding coronal medium. When the magnetic monopoles that account for the source current for the bipolar field strengthen, the upward hydromagnetic buoyancy force overcomes the downward gravitational force so that the prominence is initiated into rising motion. The illustrative examples show that prominences can move away from the solar surface by the action of the hydromagnetic buoyancy force, which is preponderant with the diamagnetic force due to the current carried by the prominence interacting with the coronal magnetic field produced by the photospheric currents, if the changes in the photospheric magnetic field are sufficiently large.

## 1. Introduction

A new dynamical model of prominence loops was recently constructed on the basis of the theory of hydromagnetic buoyancy force for flux ropes (Yeh, 1989). A prominence loop immersed in the solar atmosphere is regarded as an extraneous body in the sense that it is magnetically separated from its surrounding medium. Thus its magnetic field, mass density, temperature, and motion are quite different from those of the surrounding medium. The important feature is the polarization current induced on the periphery of the prominence that makes the ambient magnetic field tangential. The exertion of the ambient hydromagnetic pressure gives rise to the hydromagnetic buoyancy force. Its predominant constituent is the diamagnetic force which amounts to the force exerted on the currents in the prominence by the external currents that sustain the coronal magnetic field. For a prominence to be in stationary equilibrium with its surrounding medium, the hydromagnetic buoyancy force counterbalances the gravitational force exerted by the massive Sun. When the coronal magnetic field evolves, the changed diamagnetic force no longer matches the gravitational force. Once the forces become unbalanced, the prominence is initiated into motion. The evolving motion may be either upward or downward, depending on whether the hydromagnetic buoyancy force is greater or less than the gravitational force. That the evolving motion of prominence filaments is driven by the evolution of the global magnetic field has been inferred from observations (Kahler *et al.*, 1988).

*Solar Physics* 132: 335–351, 1991.

© 1991 Kluwer Academic Publishers. Printed in Belgium.

In this paper we apply the dynamical theory to study the motion of the top section of a prominence loop arched above the solar surface. The calculation presented is mathematically one-dimensional in space (viz., the heliocentric distance) although it involves two-dimensional geometry and the magnetic field is three-dimensional (see Figure 1). The governing equations for the dynamical evolution are MHD equations of motion supplemented with equations of mass conservation, flux conservation, and energy conservation. Since we are mainly interested in the dynamics of prominences, energetics is dealt with only to the extent necessary to provide a closed system of equations for the dynamics. Accordingly, in our present calculations we neglect all entropy-generating processes that are pertinent to the thermodynamics of prominences.

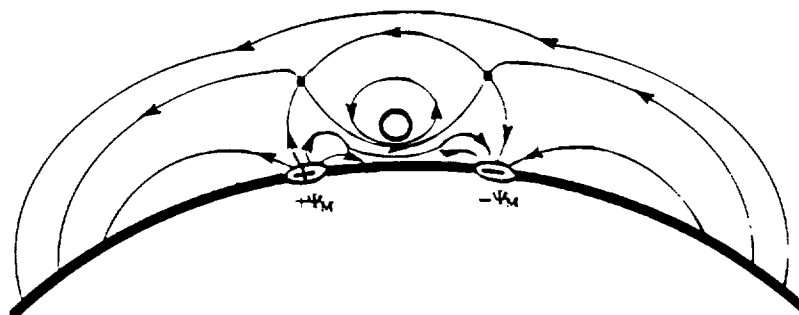


Fig. 1. Magnetic configuration resulting from the interaction between a couple of magnetic monopoles on the solar surface and a large current carried by the prominence, with a polarization current induced on the interface.

Several illustrative examples of dynamical evolution of a prominence loop are shown. First, we construct an equilibrium configuration for a prominence loop immersed in a coronal medium that has a bipolar magnetic field permeated into a magnetohydrostatic atmosphere. For a prominence loop to be stationary, it must have neither translational motion as a whole nor expansional motion relative to its axis. The former requires that the downward pull of the gravitational force exerted by the Sun is balanced by the upward lift of the hydromagnetic buoyancy force exerted by the surrounding coronal medium. The latter requires that the outward push of the force by the gas pressure and the azimuthal current of the prominence is balanced by the inward pinch of the force by the hydromagnetic pressure of the ambient medium and the axial current of the prominence. Next, we calculate the motion of the prominence loop when the equilibrium is lost because of a temporal change of the bipolar field. The change can be caused by strengthening and/or displacement of the magnetic monopoles for the bipolar field. These examples demonstrate that the prominence can move away from the solar surface when the change is sufficiently large.

The model calculations illustrate the mechanism involving hydromagnetic buoyancy force that is likely to be important in the eruption of prominences. Such calculations in conjunction with analytical study also serve to narrow down the range of the

parameters as an aid to MHD numerical simulations of the eruptive motion of prominences. Very often the difficulties with numerical simulations lie in the large number and extensive range of the pertinent parameters that characterize the phenomenon under study (Wu *et al.*, 1990).

## 2. Assumptions

The geometry of the prominence loop may be described by its axis and its cross-section. We assume that the varying cross-section is well accounted for by a circular cross-section whose radius changes in time. In this treatment of the top section of a prominence loop, a prominence is represented by a flux rope with a straight axis, whose heliocentric distance may change. The corona is represented by a magnetized medium that has a transverse magnetic field, perpendicular to the axis of the prominence, which is bipolar and a longitudinal magnetic field, parallel to the axis, which varies with the heliocentric distance only. The current that produces the bipolar field is below the solar surface; it is to be accounted for by a couple of magnetic monopoles on the photosphere. These monopoles are chosen to be line monopoles to make the problem two-dimensional. The current that produces the longitudinal magnetic field is in the corona. The coronal current is in magnetohydrostatic equilibrium with a stratified gas pressure of the coronal gas which is acted upon by solar gravity.

The prominence loop carries helical field lines. The helical magnetic field in the straight prominence is represented by

$$\mathbf{B}_E = \mathbf{1}_z B_0 \left(1 - \frac{q^2}{Q^2}\right)^{1/2} + \mathbf{1}_\phi \frac{1}{2} \mu J_0 q \quad (1)$$

in cylindrical coordinates  $(z, q, \phi)$ , with the azimuthal angle  $\phi$  measured from the radial line pointing downward ( $\mu$  being the magnetic permeability in mks units). The axial component decreases from the axial value  $B_0$  at the axis  $q = 0$  to zero at the boundary  $q = Q$ . The azimuthal component increases from zero at the axis to the boundary value  $B_B \equiv \frac{1}{2} \mu J_0 Q$  at the boundary. The total axial flux is  $\Psi_E \equiv \frac{2}{3} \pi Q^2 B_0$  and the total azimuthal flux is  $\frac{1}{3} Q^2 \mu J_0$  per unit axial length. This helical magnetic field is produced by the current density

$$\mathbf{J}_E = \mathbf{1}_z J_0 + \mathbf{1}_\phi \mu^{-1} \frac{B_0}{Q} \frac{q/Q}{(1 - q^2/Q^2)^{1/2}}, \quad (2)$$

which has an axial component that is uniform and an azimuthal component that increases from zero at the axis to infinity at the boundary. The total axial current is  $I_E \equiv \pi Q^2 J_0$  and the total azimuthal current is  $\mu^{-1} B_0$  per unit axial length. The Lorentz-force density

$$\mathbf{J}_E \times \mathbf{B}_E = \mathbf{1}_q \left( \mu^{-1} \frac{B_0^2}{Q} - \frac{1}{2} \mu J_0^2 Q \right) \frac{q}{Q} \quad (3)$$

acting at various mass elements of the prominence is in the radial direction, perpendicular to the axis of the prominence loop. It increases from zero at the axis to  $\mu^{-1} B_0^2/Q - \frac{1}{2}\mu J_0^2 Q$  at the boundary, in proportion to the radial distance. The axial current produces a pinching force toward the axis whereas the azimuthal current produces an anti-pinching force away from the axis.

The immersion of the prominence loop in the coronal medium causes a polarization current that keeps the internal field lines of the prominence separated from the external field lines of the corona. The induced current, which is concentrated in a thin peripheral layer by virtue of the high electrical conductivity of the solar plasma, produces a magnetic field that makes the ambient field tangential by cancelling the radial component of the coronal field on the interface and essentially doubling the azimuthal component there (Yeh, 1983). With the coronal mass density  $\rho_c$ , the coronal gas pressure  $p_c$ , and the coronal magnetic field  $\mathbf{B}_c \equiv \mathbf{i}_\phi B_{c\phi} + \mathbf{B}_{c\perp}$  pre-existing at the site of the prominence, the ambient magnetic field on the outer surface of the current layer is

$$\mathbf{B}_A(\phi) = \mathbf{i}_\phi B_{c\phi}|_{q=Q} + \mathbf{i}_\phi 2(\mathbf{i}_\phi \cdot \mathbf{B}_{c\perp})|_{q=Q} + \mathbf{i}_\phi \frac{\mu I_E}{2\pi Q} \quad (4)$$

The boundary magnetic field on the inner surface is

$$\mathbf{B}_B(\phi) = \mathbf{i}_\phi \frac{\mu I_E}{2\pi Q} \quad (5)$$

The polarization current, given by  $\mathbf{i}_p \equiv \mathbf{i}_\phi \mu^{-1}(\mathbf{B}_A - \mathbf{B}_B)$  per unit circumferential length, shields off the coronal field from permeating into the prominence. Across the massless layer of peripheral current the sum of gas pressure and magnetic pressure is invariant. The ambient gas pressure

$$p_A(\phi) = p_c|_{q=Q} \quad (6)$$

on the outer surface is essentially equal to the pre-existing coronal gas pressure at the periphery since the gas pressure in the exterior region is hardly perturbed by the intrusion of the prominence. The boundary gas pressure

$$p_B(\phi) = p_c|_{q=Q} + \frac{1}{2}\mu^{-1} B_{c\phi}^2|_{q=Q} + 2\mu^{-1} B_{c\perp}^2|_{q=Q} \cos^2 \phi + \frac{I_E}{\pi Q} B_{c\perp}|_{q=Q} \cos \phi \quad (7)$$

on the inner surface has a circumferential inhomogeneity which is spatially transformed from that of the ambient hydromagnetic pressure. The gas pressure inside the prominence is well represented by

$$p_E(q, \phi) = [p_0 - (p_c + \frac{1}{2}\mu^{-1} B_{c\phi}^2)|_{q=0}] \left(1 - \frac{q^2}{Q^2}\right) + p_c(q, \phi) + \frac{1}{2}\mu^{-1} B_{c\phi}^2(q, \phi) + \mu^{-1} B_{c\perp}^2(q, \phi) +$$

$$+ \mu^{-1} B_{x \perp q=0}^2 \left( 2 \frac{q^2}{Q^2} \cos^2 \phi - 1 \right) + \\ + \mu^{-1} (B_{x \perp q=Q}^2 - B_{x \perp q=0}^2) \frac{q^2}{Q^2} \cos 2\phi + \frac{I_E}{\pi Q^2} B_{x \perp q=Q} \cos \phi.$$

It varies from the axial value  $p_0$  at the axis to the boundary value  $p_B$ . The gradient of this gas pressure yields the force density

$$-\nabla p_E = -\nabla(p_x + \frac{1}{2}\mu^{-1} B_x^2 + \frac{1}{2}\mu^{-1} B_{x \perp}^2) + \mathbf{1}_r \frac{I_E B_{x \perp r=r_0}}{\pi Q^2} - \\ - \mathbf{1}_q \frac{2p_0 - (2p_x + \mu^{-1} B_x^2)_{r=r_0}}{Q} \frac{q}{Q}, \quad (9)$$

ignoring insignificant terms. The term proportional to  $q/Q$  represents a radial force density that results from the difference between the internal gas pressure and the circumferential average of the external hydromagnetic pressure. The other terms, resulting from the circumferential inhomogeneity of the ambient hydromagnetic pressure, represent the spatial spreading of the hydromagnetic buoyancy force. The latter amounts to  $\mathbf{1}_r \rho_r G M_\odot / r_0^2 + \mathbf{1}_E \times \mathbf{B}_r / \pi Q^2 + \mathbf{1}_r \Gamma \mu^{-1} B_{x \perp}^2 / R_c$  by virtue of the magneto-hydrostatic state of the coronal medium (see Equations (24) and (25) for the definitions of  $R_c$  and  $\Gamma$ ). The coefficient  $\Gamma$  has the value of 2 in the above elucidation.

The prominence moves with the velocity

$$\mathbf{u}_E = \mathbf{1}_r u_0 + \mathbf{1}_q V \frac{q}{Q}, \quad (10)$$

which consists of a translational velocity common to all mass elements of the prominence loop and an expansional velocity proportional to the distance from the axis. The translational motion is driven by the part of the force density that is uniform and the expansional motion is driven by the part of the force density that is in various radial directions. The former part includes the gravitational force exerted by the Sun and the hydromagnetic buoyancy force exerted by the surrounding medium. The latter part includes the Lorentz force that results from the interaction among the internal currents inside the prominence and the gradient force that results from the pressure difference between the internal and external gases.

The dynamical evolution of the prominence depends on its inertia. We assume that the mass density is uniform over the cross section, ignoring the higher-order effect of the spatial variation of the mass distribution. The value of mass density  $\rho_E$  changes in time.

### 3. Governing Equations

A prominence which is located initially equidistant from the two magnetic line monopoles will remain so when its heliocentric distance changes temporally (Figure 1).

The prominence loop is characterized by eight parameters:  $r_0$ ,  $Q$ ,  $u_0$ ,  $V$ ,  $\rho_E$ ,  $B_0$ ,  $J_0$ , and  $p_0$ .

The characterizing parameters evolve in accordance with the differential equations

$$\frac{d}{dt} r_0 = u_0, \quad (11)$$

$$\frac{d}{dt} Q = V, \quad (12)$$

$$\rho_E \frac{d}{dt} u_0 = -\rho_E \frac{GM_\odot}{r_0^2} - \rho_c \frac{GM_\odot}{r_0^2} + J_0 B_{c\perp} - \Gamma \frac{\mu^{-1} B_{c\perp}^2}{R_c}, \quad (13)$$

$$\rho_E \frac{d}{dt} V = \frac{2\rho_0 + \mu^{-1} B_0^2}{Q} - \frac{2\rho_c + \mu^{-1} B_{c\perp}^2}{Q} - \frac{\frac{1}{2}\mu J_0^2 Q^2}{Q}, \quad (14)$$

supplemented by the temporal invariances of total mass, axial magnetic flux, azimuthal magnetic flux, and total thermal energy:

$$\pi Q^2 \rho_E = M_E, \quad (15)$$

$$\frac{2}{3} \pi Q^2 B_0 = \Psi_E, \quad (16)$$

$$\frac{1}{4} Q^2 J_0 = \frac{1}{4\pi} I_E, \quad (17)$$

$$\frac{3}{2} \pi Q^2 + \frac{1}{2} \left[ \frac{1}{2} \rho_0 + \frac{1}{2} (\rho_c + \frac{1}{2} \mu^{-1} B_{c\perp}^2) \right] = E_E. \quad (18)$$

For a prominence to be initially in stationary equilibrium with the surrounding coronal medium the requisite current density is

$$J_0 = \frac{\rho_E - \rho_c}{B_{c\perp}} - \frac{GM_\odot}{r_0^2} - \Gamma \frac{\mu^{-1} B_{c\perp}}{R_c} \quad (19)$$

in terms of the mass density (or the requisite  $\rho_E$  in terms of the current density) and other quantities. The requisite magnetic field, in either direction, is

$$B_0 = \pm (2\mu\rho_c + B_{c\perp}^2 - \frac{1}{2}\mu^2 J_0^2 Q^2 - 2\mu\rho_0)^{1/2} \quad (20)$$

in terms of the gas pressure (or the requisite  $\rho_0$  in terms of the magnetic field) and other quantities. The first constraint makes the upward hydromagnetic buoyancy force exactly balance the downward gravitational force. The second constraint makes the outward forces due to the gas pressure and the azimuthal current of the prominence exactly balance the inward forces due to the hydromagnetic pressure of the ambient medium and the axial current of the prominence. These two constraints are depicted in Figures 2 and 3, which show the required values of  $\frac{1}{2}\mu Q J_0$  and  $B_0$  for various values of  $r_0$ ,  $Q$ ,  $\rho_E$ ,  $\rho_0$ ,  $\rho_c$ ,  $T_c$ ,  $B_{c\parallel}$ , and  $B_{c\perp}$ , in the neighborhood of the equilibrium values used in the examples (see Section 6).

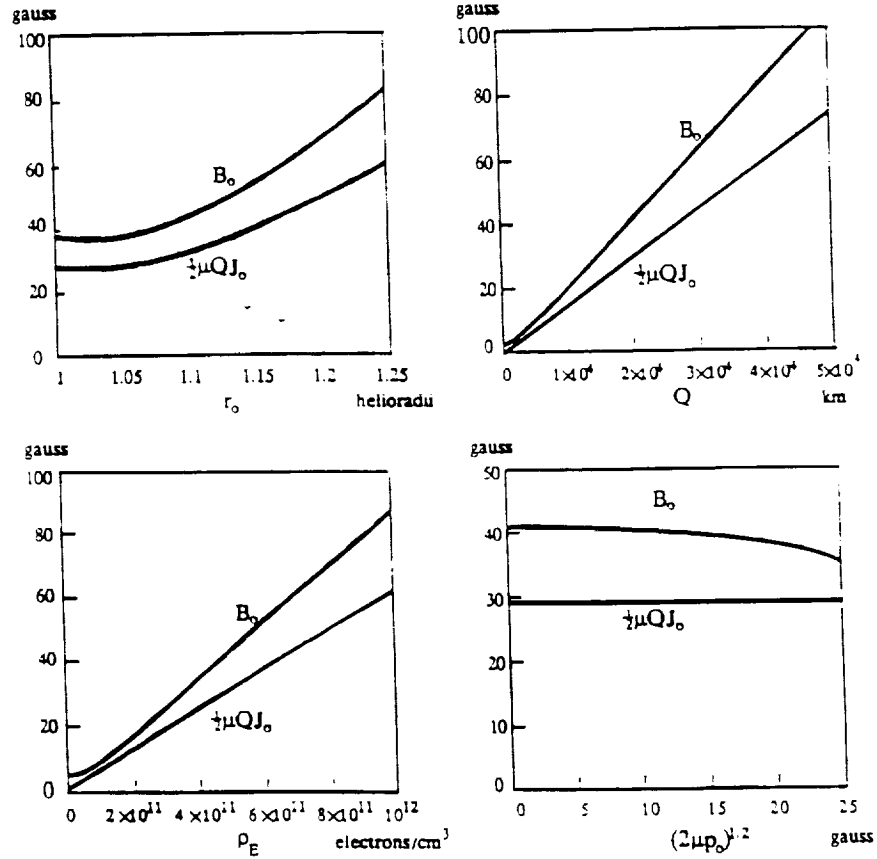


Fig. 2. Required values of  $\frac{1}{2}\mu Q J_0$  and  $B_0$  for an equilibrium prominence with various values of  $r_0$ ,  $Q$ ,  $\rho_E$ , or  $\rho_0$ .

#### 4. Coronal Medium

We choose the line monopoles for the bipolar magnetic field to have strengths of  $\pm \Psi_M$  and angular separation of  $2\theta_M$ . The two monopoles produce the bipolar magnetic field

$$B_{\pm} = \mathbf{1}_r B_{\pm} \quad (21)$$

in the midplane between them. Its direction, from the positive monopole to the negative monopole, is perpendicular to the midplane. Its magnitude is

$$B_{\pm} = \frac{\Psi_M}{\pi} \frac{R_\odot \sin \theta_M}{r^2 - 2rR_\odot \cos \theta_M + R_\odot^2} \quad (22)$$

at a heliocentric distance of  $r$ . There the associated magnetic pressure has the gradient

$$-\nabla_{\pm} \mu^{-1} B_{\pm}^2 = \mathbf{1}_r \frac{\mu^{-1} B_{\pm}^2}{R_c} \quad (23)$$



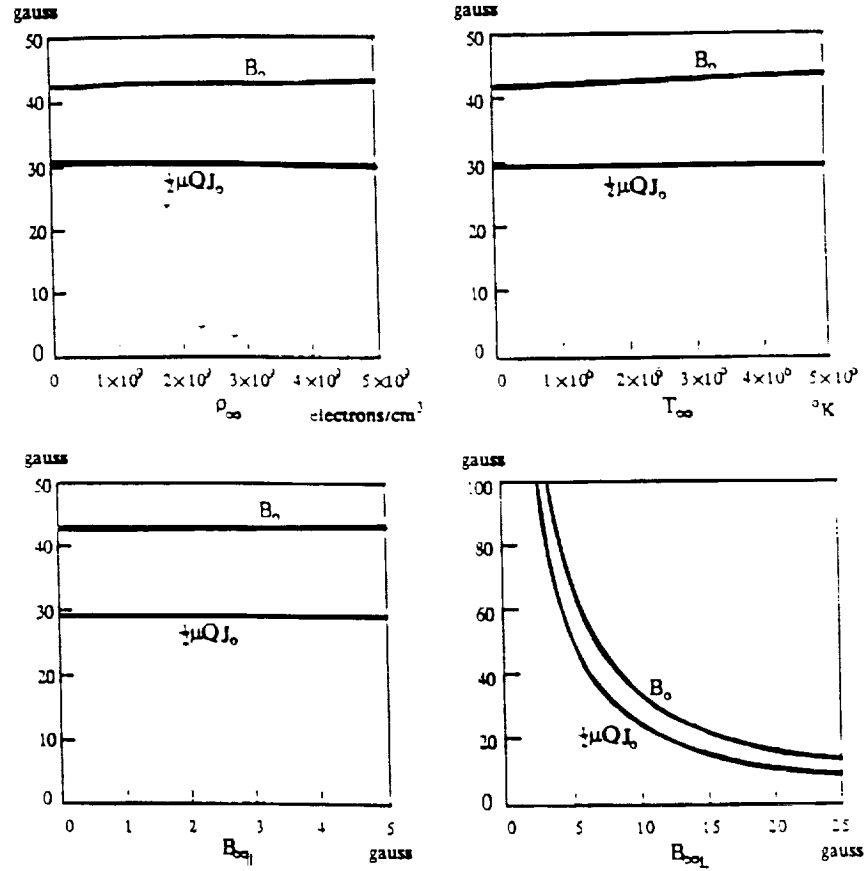


Fig. 3. Required values of  $\frac{1}{2}\mu Q J_0$  and  $B_0$  for an equilibrium prominence in a coronal medium with various values of  $\rho_\infty$ ,  $T_\infty$ ,  $B_{eq1}$ , or  $B_{\infty 1}$ .

in the vertical direction, with the radius-of-curvature

$$R_c = \frac{r^2 - 2rR_\infty \cos \theta_{Mf} + R_\infty^2}{r - R_\infty \cos \theta_{Mf}} \quad (24)$$

for the circular field line. (By virtue of the current-freeness of the bipolar field, the gradient force of its magnetic pressure is exactly opposite to its tensile force density.) This magnetic pressure gradient is enhanced by a factor

$$\Gamma = \frac{2}{(1 - Q^2/q_{Mf}^2)[(1 - Q^2/q_{Mf}^2)^2 + 4(Q^2/q_{Mf}^2) \sin^2 \phi_{Mf}]} \quad (25)$$

by the polarization current

$$i_P = \frac{1}{\mu} B_{c \perp} \frac{2q_{Mf}^2(Q^2 + q_{Mf}^2) \cos \phi - 4Qq_{Mf}^3 \cos \phi_{Mf}}{[Q^2 - 2Qq_{Mf} \cos(\phi - \phi_{Mf}) + q_{Mf}^2][Q^2 - 2Qq_{Mf} \cos(\phi + \phi_{Mf}) + q_{Mf}^2]} \quad (26)$$

Here  $q_M \equiv (r_0^2 - 2r_0R_\odot \cos \theta_M + R_\odot^2)^{1/2}$  is the distance from the prominence to either monopole and  $\phi_M \equiv \arcsin(R_\odot \sin \theta_M / q_M)$  is the azimuthal angle for the monopole. The field strength  $B_{\perp \infty}$  increases with  $\Psi_M$  and becomes maximized when  $\cos \theta_M$  is equal to  $2rR_\odot / (r^2 + R_\odot^2)$ . In terms of the field strength on the solar surface midway between the two monopoles, the monopole strength has the value

$$\Psi_M = 2\pi \frac{1 - \cos \theta_M}{\sin \theta_M} R_\odot B_{\perp \infty, r=R_\odot}. \quad (27)$$

The monopole strength  $\Psi_M$  and the separation angle  $2\theta_M$  may undergo temporal changes.

We choose the longitudinal magnetic field

$$B_{\parallel} = 1_z B_r \quad (28)$$

produced by the coronal current to be horizontal. The associated current density is  $1_r \mu^{-1} dB_r / dr$ . It provides a magnetic force in the force balance

$$-\frac{d}{dr} \left( p_{\perp} + \frac{1}{2} \mu^{-1} B_r^2 \right) = p_{\perp} \frac{GM_\odot}{r^2} \quad (29)$$

between the gravitational force and the gradient of hydromagnetic pressure. In addition to the equation of force balance, two more constraints are needed in order to determine the vertical variation of the coronal mass density, gas pressure, and longitudinal magnetic field. We shall assume that the gas pressure varies in proportion to the mass density and the magnetic pressure varies in proportion to the gas pressure, viz.,

$$p_{\perp} = \frac{p_{\perp, r=R_\odot}}{\rho_{\perp, r=R_\odot}} \rho_{\perp}, \quad (30)$$

$$B_r^2 = \frac{B_{r=R_\odot}^2}{p_{\perp, r=R_\odot}} p_{\perp}. \quad (31)$$

These assumptions ensure that the pressure and mass density decrease with the heliocentric distance. They allow us to calculate the mass density by numerical integration of the differential equation

$$\frac{d}{dr} \rho_{\perp} = - \frac{1}{1 + \frac{1}{2} \mu^{-1} B_{r=R_\odot}^2 / p_{\perp, r=R_\odot}} \frac{GM_\odot}{KT_{\perp}} \frac{\rho_{\perp}}{r^2} \quad (32)$$

from the solar surface. The ratio  $p_{\perp} / \rho_{\perp}$  divided by the gas constant of the solar plasma is the constant temperature  $T_{\perp}$  of the coronal medium.

### 5. Conditions for Upward and Outward Accelerations

In order for the translational motion to have an upward acceleration away from the Sun, the hydromagnetic buoyancy force must overcome the gravitational force. The former

will exceed the latter if the bipolar field is sufficiently large so that

$$B_{c\perp} > \frac{1}{\frac{1}{2} + [\frac{1}{4} + \Gamma\mu^{-1}GM_{\odot}(\rho_E - \rho_{\infty})/r_0^2J_0^2R_c]^{1/2}} \frac{GM_{\odot}}{r_0^2} \frac{\rho_E - \rho_{\infty}}{J_0}. \quad (33)$$

On the other hand, in order for the expansional motion to have an outward acceleration away from the axis, the outward force must overcome the inward force. The former will exceed the latter if the surrounding medium has a hydromagnetic pressure sufficiently small so that

$$p_{\infty} + \frac{1}{2}\mu^{-1}B_{c\perp}^2 < p_0 + \frac{1}{2}\mu^{-1}B_0^2 - \frac{1}{4}\mu J_0^2Q^2. \quad (34)$$

Upon the use of the equilibrium values at  $t = 0$  and the conservation invariants, the condition for upward acceleration can be written as

$$B_{c\perp} > B_{c\perp}|_{t=0} \left( \frac{r_0|_{t=0}}{r_0} \right)^2 \frac{1 - (\rho_{\infty}/\rho_E|_{t=0})(Q/Q|_{t=0})^2}{1 - \rho_{\infty}|_{t=0}\rho_E|_{t=0}} \quad (35)$$

if we ignore the higher-order part of the diamagnetic force associated with the pre-existing gradient of the coronal magnetic pressure. The condition for outward acceleration can be written as

$$p_{\infty} + \frac{1}{2}\mu^{-1}B_{c\perp}^2 < \left\{ p_{\infty}|_{t=0} + \frac{1}{2}\mu^{-1}B_{c\perp}^2|_{t=0} + \frac{1}{4}\mu^{-1}B_0^2|_{t=0} \left[ \left( \frac{Q|_{t=0}}{Q} \right)^{2/3} - 1 \right] + \right. \\ \left. + \frac{1}{8}\mu J_0^2|_{t=0} Q^2|_{t=0} \left[ 1 - \left( \frac{Q}{Q|_{t=0}} \right)^{4/3} \right] \right\} \left( \frac{Q|_{t=0}}{Q} \right)^{2+4/3}. \quad (36)$$

It follows from the inequality (35) that in the region where  $\rho_{\infty}$  is small, the translational motion will have an upward acceleration when the bipolar magnetic field encountered.  $B_{c\perp}(t)$  is not less than its initial value by a factor of  $(r_0|_{t=0}/r_0)^2$ . On the other hand, it follows from the inequality (36) that the expansional motion will have an outward acceleration in the region where  $p_{\infty} + \frac{1}{2}\mu^{-1}B_{c\perp}^2$  is less than its initial value when  $Q(t)$  is less than  $Q|_{t=0}$  and in the region where  $p_{\infty} + \frac{1}{2}\mu^{-1}B_{c\perp}^2$  is sufficiently less than its initial value when  $Q(t)$  is greater than  $Q|_{t=0}$ .

## 6. Examples

In mks units, the magnetic permeability has the value  $\mu = 4\pi \times 10^{-7} \text{ T}^2 \text{ m}^3 \text{ J}^{-1}$ , the gravitational constant times solar mass has the value

$$GM_{\odot} = (6.67 \times 10^{-11} \text{ N m}^2 \text{ kg}^{-2}) \times (1.99 \times 10^{30} \text{ kg}),$$

and the gas constant for the proton-electron plasma has the value

$$K = (1.38 \times 10^{-23} \text{ J deg}^{-1}) \frac{1}{2} (1.67 \times 10^{-27} \text{ kg} + 9.11 \times 10^{-31} \text{ kg}).$$

To facilitate the numerics, we choose to measure time, length, and magnetic field in the units of 1 hour, one helioradius, and 1 G, respectively, viz.,  $t_{\text{ref}} = 3.6 \times 10^3$  s,  $r_{\text{ref}} = 6.96 \times 10^8$  m, and  $B_{\text{ref}} = 10^{-4}$  T. We further choose to measure speed, mass density, pressure, current density, and temperature in the units of  $r_{\text{ref}}/t_{\text{ref}}$ ,  $(\mu^{-1} B_{\text{ref}}^2) (r_{\text{ref}}/t_{\text{ref}})^2$ ,  $\mu^{-1} B_{\text{ref}}^2$ ,  $\mu^{-1} B_{\text{ref}}/r_{\text{ref}}$ , and  $(r_{\text{ref}}/t_{\text{ref}})^2/K$ . Namely,  $u_{\text{ref}} = 193.3$  km s $^{-1}$ ,  $\rho_{\text{ref}} = 2.129 \times 10^{-13}$  kg m $^{-3}$  (corresponding to  $1.274 \times 10^8$  electrons cm $^{-3}$ ),  $p_{\text{ref}} = 7.958 \times 10^{-3}$  J m $^{-3}$ ,  $J_{\text{ref}} = 1.143 \times 10^{-7}$  A m $^{-2}$ , and  $T_{\text{ref}} = 2.263 \times 10^6$  deg. In these normalized units, henceforth, both the magnetic permeability, given by

$$(4\pi \times 10^{-7} \text{ T}^2 \text{ m}^3 \text{ J}^{-1}) (B_{\text{ref}}^2 J_{\text{ref}} r_{\text{ref}}),$$

and the gas constant, given by

$$(1.65 \times 10^4 \text{ J kg}^{-1} \text{ deg}^{-1}) (u_{\text{ref}}^2 T_{\text{ref}}),$$

have the value of unity whereas the gravitational constant times solar mass has the value of 5.102 helioradius $^3$  h $^{-2}$ , given by  $(1.333 \times 10^{20} \text{ m}^3 \text{ s}^{-2})/(r_{\text{ref}} u_{\text{ref}}^2)$ .

For the magnetohydrostatic coronal atmosphere, we choose a mass density of  $3 \times 10^9$  electrons cm $^{-3}$ , a temperature of  $2 \times 10^6$  K (hence,  $T_{\infty} = 0.8838$ ) and a longitudinal magnetic field of 2 G at the solar surface. For the magnetic monopoles, to have a transverse magnetic field of 10 G at the solar surface midway between the two

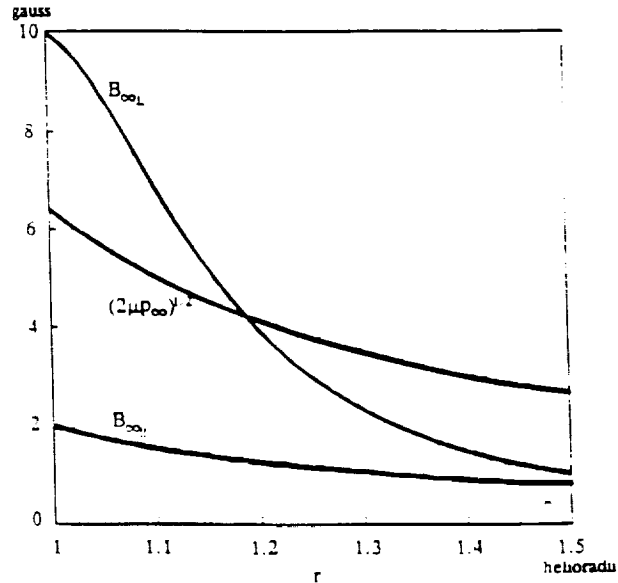


Fig. 4. Profile of a stratified magnetohydrostatic corona at  $2 \times 10^6$  K, with a mass density of  $3 \times 10^9$  electrons cm $^{-3}$ , a longitudinal magnetic field of 2 G, and a transverse magnetic field of 10 G at the solar surface.

monopoles, we choose

$$\Psi_M = 5.497 \text{ G helioradius, } \theta_M = 10^\circ.$$

The calculated profiles are shown in Figure 4.

For a stationary prominence loop, we choose a height of  $5 \times 10^4$  km, a radius of  $2 \times 10^4$  km, a mass density of  $5 \times 10^{11}$  electrons  $\text{cm}^{-3}$ , and a temperature of  $5 \times 10^4$  K so that:

$$r_0 = 1.0718, \quad Q = 0.02874, \quad \rho_E = 3924.2, \quad p_0 = 86.704.$$

At the site where the prominence resides we have

$$\rho_{\pi} = 16.535, \quad \rho_{\pi} = 14.614, \quad B_{\pi} = 1.676, \quad B_{\pi\perp} = 8.054.$$

The conditions of force balance require

$$J_0 = 2080.9, \quad B_0 = 40.574.$$

In other words, for the prominence loop to be in stationary equilibrium with the surrounding medium, it must carry a total axial current  $I_E$  of  $3.0 \times 10^{11}$  A and carry an azimuthal current that sustains a total axial magnetic flux  $\Psi_E$  of  $3.4 \times 10^{12}$  webers. These values are within the range of typical values for quiescent prominences

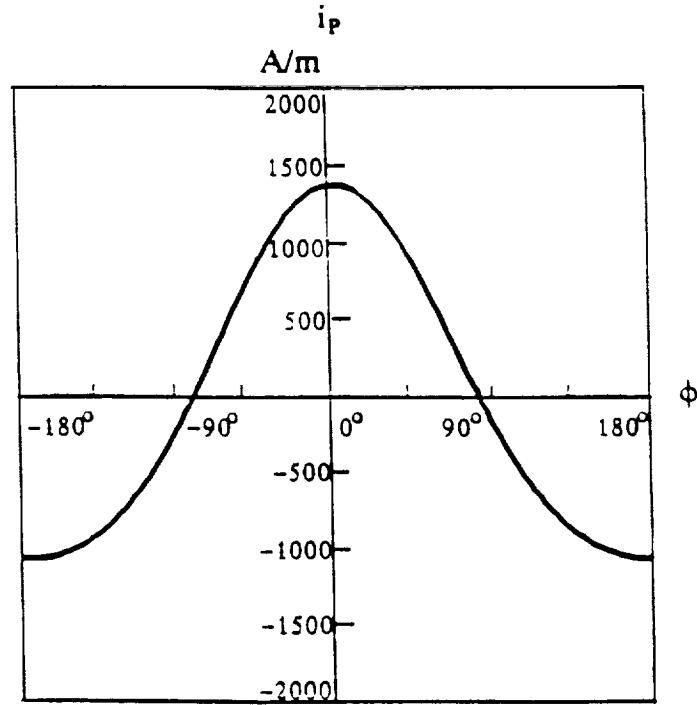


Fig. 5. Peripheral distribution of the polarization current in the equilibrium configuration.

(Tandberg-Hanssen, 1974). It is seen from

$$\rho_E \frac{GM_\odot}{r_0^2} = 17428.7, \quad \rho_\infty \frac{GM_\odot}{r_0^2} = 73.61, \quad \frac{I_E B_{\infty \perp}}{\pi Q^2} = 16759.7,$$

$$\Gamma \frac{\mu^{-1} B_{\infty \perp}^2}{R_c} = 595.4$$

that the gravitational force is largely balanced by the diamagnetic force (the part due to the inhomogeneity of the coronal magnetic field is only 3.55% of the part due to the prominence current). The hydrostatic buoyancy force is very small, accounting for only 0.42%. On the other hand, it is seen from

$$p_0 = 86.704, \quad \frac{1}{2} \mu^{-1} B_0^2 = 823.14, \quad \frac{1}{2} \mu J_0^2 Q^2 = 893.82,$$

$$p_\infty = 14.615, \quad \frac{1}{2} \mu^{-1} B_\infty^2 = 1.405$$

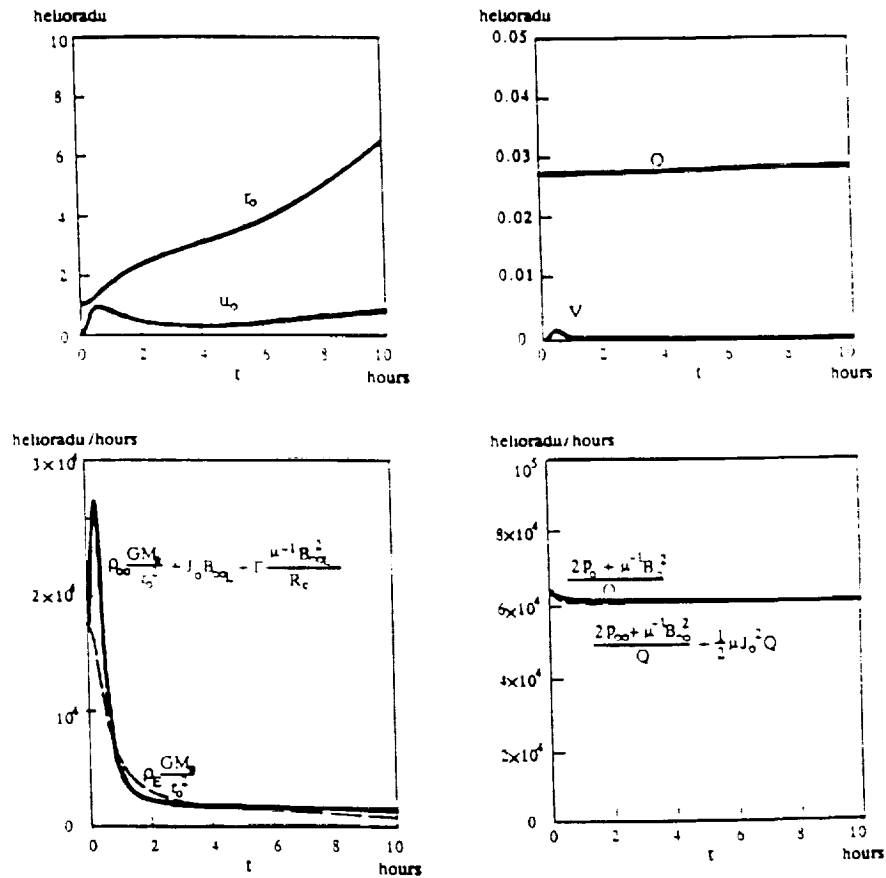


Fig. 6. Evolution of the prominence as the monopole strength increases, with  $d\Psi_r/dr = 20$  G helioradius  $h^{-1}$ .

that the pinching force of the axial current is largely balanced by the anti-pinching force of the azimuthal current and to a lesser extent by the internal gas pressure. The ambient hydromagnetic pressure provides only a very small pinching. To facilitate comparison, these values may be translated to  $(2\mu p_z)^{1/2} = 5.4063$  G,  $\frac{1}{2}\mu J_0 Q = 29.903$  G, and  $(2\mu p_0)^{1/2} = 13.168$  G. The plasma beta at the axis is 0.1053. The transverse projection of the field lines in the equilibrium configuration is as shown in Figure 1. With the ratio  $\mu I_E/\Psi_M = 0.9684$ , the bipolar field has two neutral points located at  $q = 0.187$ ,  $\phi = \pm 118.7^\circ$ . Figure 5 shows the peripheral distribution of the polarization current with  $q_M = 0.194$  and  $\phi_M = 63.4^\circ$ . The polarization current flows in the direction of the prominence current in the lower periphery ( $\phi < 82.6^\circ$ ) and flows in the opposite direction in the upper periphery. It is zero at the two points where the two neutral points would be located in the case  $I_F$  happens to be zero. Of course, the total polarization current sums up to zero.

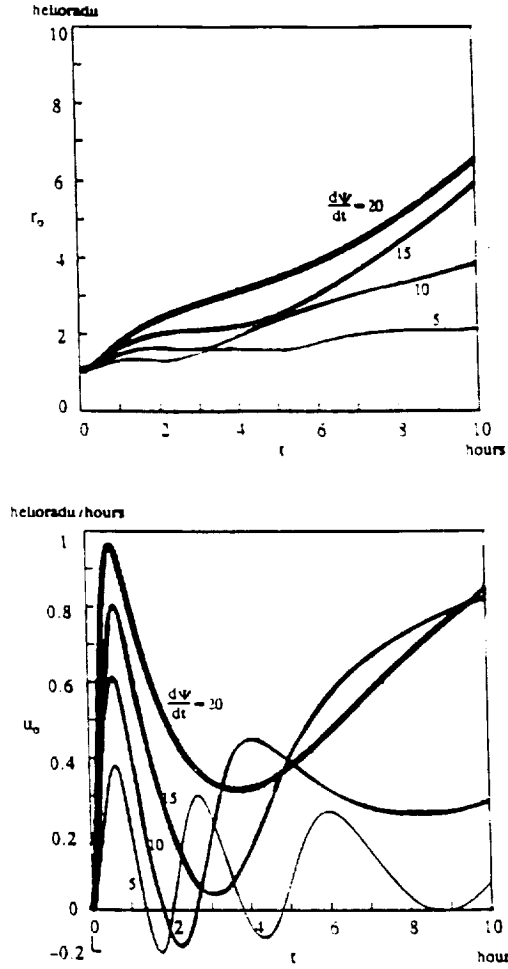


Fig. 7. Evolution of the prominence with various values of  $d\Psi_M/dt$ .

Now, we consider the motion of the prominence loop when the equilibrium is lost. The initiated motion is caused by a temporal change of the bipolar magnetic field due to the strengthening of the monopoles. Figure 6 shows the evolution with

$$\frac{d}{dt} \Psi_M = 20.0 \text{ G helioradius h}^{-1} \quad \text{for } 0 < t < 10 \text{ h},$$

revealed by the numerical solution of the dynamical equations. The initial increase in the bipolar field makes the hydromagnetic buoyancy force exceed the gravitational force, so that the prominence rises from its equilibrium position. The prominence keeps moving upward, even during the short while  $0.6 < t < 3.5$  when the prominence is decelerated because the hydromagnetic buoyancy force is not large enough to exceed the gravitational force. Likewise, the radius of the prominence keeps increasing. Its rate of increase is small in this case because the encountered coronal hydromagnetic pressure decreases very slowly. To see the dependence on the speed of the evolution of the photospheric magnetic field, we show in Figure 7 the evolution caused by smaller values of  $d\Psi_M/dt$ . It is seen that the prominence may move up and down in oscillational motion if the evolution is slow. With a sufficiently rapid evolution, the prominence will move away from the Sun. In passing, we mention that the prominence would move downward in response to negative values of  $d\Psi_M/dt$ .

## 7. Discussion

The calculations show the importance of the hydromagnetic buoyancy force, which includes the diamagnetic force, in the dynamics of prominence loops. In the illustrative examples, not only in equilibrium but also during the motion, the hydromagnetic buoyancy force is preponderant with the diamagnetic force due to the current carried by the prominence interacting with the coronal magnetic field produced by the photospheric currents. The part of the diamagnetic force due to the inhomogeneity of the coronal magnetic field only amounts to a few percent and the hydrostatic buoyancy force is even much smaller. Their percentages diminish in heliocentric distance. Therefore, we conclude that without the action of the diamagnetic force due to the prominence current, prominences are not likely to move away from the solar surface.

In fact, when the prominence is close to the photospheric surface, the diamagnetic force is enhanced by the mirror-current effect (Kuperus and Raadu, 1974). The polarization current induced on the photosphere will exert an additional upward force on the prominence current in the amount of  $\mu I_E^2 R_\odot^2 / (2\pi r_0(r_0^2 - R_\odot^2))$  (cf. Van Tend and Kuperus, 1978). Inclusion of this force will modify Equation (13) to

$$\begin{aligned} \rho_E \frac{d}{dt} u_0 = & -\rho_E \frac{GM_\odot}{r_0^2} + \rho_\infty \frac{GM_\odot}{r_0^2} + J_0 B_{x\perp} - \Gamma \frac{\mu^{-1} B_{x\perp}^2}{R_c} + \\ & + \mu J_0^2 \frac{Q^2 R_\odot^2}{2r_0(r_0^2 - R_\odot^2)}. \end{aligned} \quad (37)$$



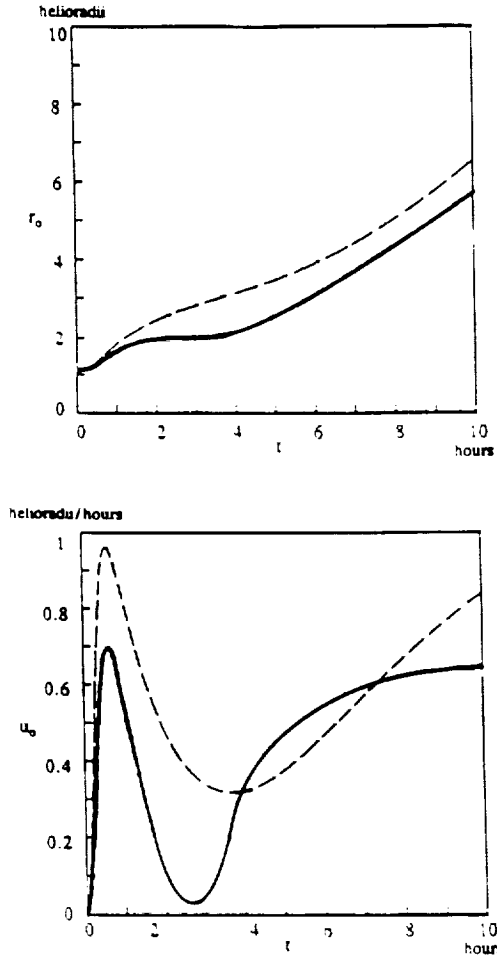


Fig. 8. Evolution of the prominence when the mirror-current effect is included in the hydromagnetic diamagnetic force, with  $d\Psi_{\text{eff}}/dt = 20$  G helioradius  $\text{h}^{-1}$ . Dashed lines indicate the corresponding evolution without the mirror currents.

Accordingly, for the prominence in the illustrative examples, the requisite current density reduces to  $J_0 = 1426.5$  and the requisite magnetic field reduces to  $B_0 = 26.44$ . With the monopoles strengthening at the rate of  $d\Psi_{\text{eff}}/dt = 20$ , the prominence rises slightly slower. See Figures 8. This is due to a smaller prominence current. The reduced  $I_E B_{\infty \perp}$  is not sufficiently compensated by the added  $\mu I_E^2 R_0^2 / 2\pi r_0 (r_0^2 - R_0^2)$ . This calculation serves as an *a posteriori* justification for the simplified model by Van Tend and Kuperus (1978).

The dynamical model illustrated by the calculations presented in this paper applies to prominence eruptions driven by gradual evolution of the photospheric magnetic field in weak field regions. It also applies to filament eruptions in active regions, with other parameter values.

### Acknowledgements

The authors thank Dr Ernest Hildner and Dr Petrus Martens for some useful suggestions. This work was supported by U.S. Air Force Office of Scientific Research under contract AFOSR-88-0013 and NAGW-5 (NASA)

### References

- Kahler, S. W., Moore, R. L., Kane, S. R., and Zirin, H.: 1988, *Astrophys. J.* **328**, 824.  
Kuperus, M. and Raadu, M. A.: 1974, *Astron. Astrophys.* **31**, 189.  
Tandberg-Hanssen, E.: 1974, *Solar Prominences*, D. Reidel Publ. Co., Dordrecht, Holland.  
Van Tend, W. and Kuperus, M.: 1978, *Solar Phys.* **59**, 115.  
Wu, S. T., Bao, J. J., Ahn, S. H., and Tandberg-Hanssen, E.: 1990, *Solar Phys.* **125**, 277.  
Yeh, T.: 1983, *Astrophys. J.* **264**, 630.  
Yeh, T.: 1989, *Solar Phys.* **124**, 251.